Dieses Dokument ist eine Zweitveröffentlichung (Verlagsversion) /

This is a self-archiving document (published version):

I. G. Gonzalez-Martinez, A. Bachmatiuk, V. Bezugly, J. Kunstmann, T. Gemming,
Z. Liu, G. Cuniberti, M. H. Rümmeli

Electron-beam induced synthesis of nanostructures: a review

Diese Version ist verfügbar / This version is available on:

https://nbn-resolving.org/urn:nbn:de:bsz:14-qucosa2-363628

SLUB
Wir führen Wissen.

TECHNISCHE UNIVERSITÄT DRESDEN

QUCOSA
Quality Content of Saxony

Electron-beam induced synthesis of nanostructures: a review

I. G. Gonzalez-Martinez,[b,c] A. Bachmatiuk,[b,d] V. Bezugly,[c] J. Kunstmann,[c,e]
T. Gemming,[b] Z. Liu,[f] G. Cuniberti[c] and M. H. Rümmeli*[a,b,d]

As the success of nanostructures grows in modern society so does the importance of our ability to control their synthesis in precise manners, often with atomic precision as this can directly affect the final properties of the nanostructures. Hence it is crucial to have both deep insight, ideally with real-time temporal resolution, and precise control during the fabrication of nanomaterials. Transmission electron microscopy offers these attributes potentially providing atomic resolution with near real time temporal resolution. In addition, one can fabricate nanostructures *in situ* in a TEM. This can be achieved with the use of environmental electron microscopes and/or specialized specimen holders. A rather simpler and rapidly growing approach is to take advantage of the imaging electron beam as a tool for *in situ* reactions. This is possible because there is a wealth of electron specimen interactions, which, when implemented under controlled conditions, enable different approaches to fabricate nanostructures. Moreover, when using the electron beam to drive reactions no specialized specimen holders or peripheral equipment is required. This review is dedicated to explore the body of work available on electron-beam induced synthesis techniques with *in situ* capabilities. Particular emphasis is placed on the electron beam-induced synthesis of nanostructures conducted inside a TEM, *viz.* the e-beam is the sole (or primary) agent triggering and driving the synthesis process.

a College of Physics, Optoelectronics and Energy & Collaborative Innovation Center of Suzhou Nano Science and Technology, Soochow University, Suzhou 215006, China. E-mail: mhr1@ifw-dresden.de

b IFW Dresden, Institute for Complex Materials, P.O. Box, D-01171 Dresden, Germany

c Institute of Materials Science and Max Bergmann Center of Biomaterials, Dresden University of Technology, 01062 Dresden, Germany

d Centre of Polymer and Carbon Materials, Polish Academy of Sciences, M. Curie-Sklodowskiej 34, Zabrze 41-819, Poland

e Theoretical Chemistry, Department of Chemistry and Food Chemistry, Dresden University of Technology, 01062 Dresden, Germany

f Center for NanoChemistry, Beijing National Laboratory for Molecular Sciences, College of Chemistry and Molecular Engineering, Peking University, Beijing 100871, China

Introduction

The miniaturization of technological appliances is a force that has been driving a large fraction of the scientific enterprise for at least the last 50 years. A vast body of techniques has been developed in order to produce the nanometer-sized components that need to be assembled into potential functional devices. Unfortunately, most of these techniques are carried out within closed chambers and thus are not suited to perform real-time observations of the growth process, instead, the synthesized products must be analyzed *ex situ* and the growth mechanism is inferred from their physical and chemical characteristics. However, there is a family of synthesis methods that is tailored to allow for *in situ* studies and even manipulations of the nanostructure's growth/formation process in real-time. Within this group of methods there is a subset that employs an electron beam as the fundamental tool to drive the growth reaction. Synthesis procedures that use the electron beam of electron microscopes, particularly the transmission electron microscope (TEM), are particularly valuable since the microscopes allow one to peer into the microstructural evolution of the products as they are being synthesized.

This review is dedicated to explore the body of work available on electron-beam induced synthesis techniques with *in situ* capabilities. Particular emphasis is placed on the electron beam-induced synthesis of nanostructures conducted inside a TEM, *viz.* the e-beam is the sole (or largely main) agent triggering and driving the synthesis process. This criterion excludes well-established techniques performed inside TEMs such as: electron-beam induced deposition (EBID)[1–4] and thermally assisted beam induced crystallization[5,6] since they require significant hardware add-ons (gas supplies, flow-cells and holders with heating stages) to assist the action of the e-beam in order to proceed successfully. The "*in situ*" requirement also filters out techniques such as electron-beam lithography[7,8] since they are not "*in situ* compatible". Topical reviews about

electron beam nanofabrication through methods such as EBID and nanolithography already exist.[9]

There is a large number of materials that are susceptible to be transformed, either globally or locally, into nanostructures of different "dimensionality" once they are subjected to a systematic electron beam irradiation procedure. Thus there are electron beam-induced methods for the production of nanoparticles ("zero" dimensions), nanowires/nanotubes/whiskers ("one" dimension) and the engineering of films ("two" dimensions) with a well-determined shape. In some cases exotic nanostructures with fractal geometries such as nano-trees or nano-dendrites can also be produced. The exact morphology of the final products depends on a combination of two main factors: the precursor's (specimen) properties (composition, melting point, atomic weight, *etc.*) and the e-beam manipulation protocol (acceleration voltage, total current, current density, *etc.*).

This review organizes the many *in situ* electron beam-induced protocols in four main sections depending on the dimensionality of the products: bulk, 2D materials, 1D materials, 0D materials and other geometries. The works presented in each category are grouped according to the similarities among the physical processes that drive their synthesis procedures.

The following section deals with the electron beam–specimen interactions that are essential to understand the physical background behind the growth mechanisms put forward by the experimenters.

Electron beam–specimen interactions

Knock-on displacement and sputtering

The laws of energy and momentum conservation establish that beam electrons must transfer a fraction of their energy when-ever they collide against a nucleus of the specimen. After the event has taken place the electron is scattered at an angle θ relative to its original trajectory. Classically, the amount of transferred energy (in eV) during the scattering event is given by:[10]

$$E = E_{\max} \sin^2(\theta/2)$$
$$E_{\max} = E_0(1.02 + E_0/10^6)/(465.7A) \tag{1}$$

where E_0 is the energy of the incoming electron in eV and A is the atomic number of the impacted nucleus. Small scattering angles are related to a small amount of transferred energy from the electron to the nucleus, indeed, small enough so as to be treated as negligible, thus, such events are generally regarded as "elastic". As the scattering angle increases so does the transferred energy reaching a maximum value at $\theta = 180°$, *i.e.* head-on collisions. In this situation the transferred energy E equals the maximum amount of energy $E_{\max}$ that an electron is able to transmit to the nucleus. $E_{\max}$ can be of several eV for highly energetic electrons colliding against low-weight nuclei.

Collision events can result in more than simple electron scattering, nuclei in the specimen can be irreversibly displaced if the transferred energy surpasses the so-called displacement energy E_d of the material. The displacement energy is characteristic of the material; not only of its chemical composition but it is highly dependent on its atomic structure. For example, graphite has an E_d of around 30 eV which is achievable by 140 keV electrons while in diamond E_d is around 80 eV and can be attainable by electrons with a kinetic energy of at least 330 keV.[11]

In the bulk, atomic displacements require a transferred energy of around 10–50 eV, they can be observed in light atomic weight specimens hit by 100 keV electrons.[12] Heavier

Ignacio Gonzalez-Martinez studied physics at the National Autonomous University of Mexico (UNAM). He obtained a Master degree on Nanobiophysics at the Dresden University of Technology (TUD), Germany. Currently he is working at the Leibniz Institute for Solid State and Materials Research, Dresden, Germany.

I. G. Gonzalez-Martinez

Gianaurelio Cuniberti studied physics at the University of Genoa and then at the University of Hamburg. He was a visiting scientist at the Massachusetts Institute of Technology (MIT) and the Max Planck Institute for the Physics of Complex Systems, Dresden. He led a Volkswagen Foundation Independent Research Group in the University of Regensburg from 2003 to 2007. Currently, he leads the chair of Materials Science and

G. Cuniberti

Nanotechnology at the Dresden University of Technology and the Max Bergmann center of Biomaterials and he is Adjunct Professor of Chemistry at the University of Alabama and the founding Director of the Dresden Center for Computational Materials Science (DCMS), Dresden. He has been awarded an Honorary Professorship at the division of IT Convergence Engineering, POSTECH, the Pohang University of Science and Technology.

elements in bulky samples require faster electron beams in order to be displaced. However, if the atoms are at the specimen's surface, their displacement energy becomes greatly reduced since they are under-coordinated (form less bonds) with respect to their counterparts within the bulk.

Surface atoms that are exposed to the vacuum can be effectively sputtered away from the specimen. In the case of atomic sputtering the displacement energy is sometimes equated to the sublimation energy per atom E_{sub}. Although an approximation given by $E_d = (5/3)E_{sub}$ can also be found in the literature.[12] While this approximation seems to work better for materials such as Nb, Mo, Au and Ag but does not do as well for materials with covalent bonding such as carbon nanotubes where the $E_d = E_{sub}$ works better.[13]

Taking $E_d = E_{sub}$ and using eqn (1) one can estimate that 300 kV electrons are able to sputter targets made of any elemental composition.[10] Thus, sputtering of specimens is routinely observed in a TEM working at acceleration voltages between 100–300 KV. Condensing the electron beam intensifies the sputtering rate. It is estimated that a sputtering rate of around 6 atomic monolayers per second is to be expected for a target composed of an element with a sputtering cross section of 100 barn irradiated with an electron beam of 100–300 kV and a current density of 10^4 A cm^{-2} (an experimental condition easily attainable in any TEM).[12]

While sputtering is typically a nuisance for observation purposes it can be turned into a valuable tool for engineering purposes, as in the selective removal of atoms from few layer graphene with a highly focused STEM beam probe scanning over pre-programmed trajectories.[14]

The Knotek–Feibelman mechanism and oxide reduction

One of the key observations that led to the formulation of the K–F mechanism was the fact that the desorbed species had

Mark H. Rümmeli obtained his PhD from the London Metropolitan University. He then worked at the German Aerospace Center (DLR) at the Institute of Space Sensor Technology and Planetary Exploration. Currently, he heads an electron microscopy group at the Department of Physics, Optoelectronics and Energy at Soochow University, China. He also oversees the Molecular Nanostructures group at the Leibniz Institute for Solid State and Materials Research, Dresden, and a gas sensor lab at the Polish Academy of Sciences. His research focuses on understanding the growth mechanisms of nanostructures, developing techniques for their functionalization and their eventual application in electronic, biomedical and energy storage technologies.

M. H. Rümmeli

experienced a change on their charges.[15] Atoms like fluorine and oxygen that are nominally bonded as F$^-$ in CF$_4$ and O^{2-} in TiO$_2$ are detected as F$^+$ and O$^+$ when they are detached from their respective parent specimens.[16] Essentially, what the K–F mechanism explains is how this charge inversion is induced and it leads to radiolysis and desorption.

Take the case of a TiO$_2$ specimen irradiated by an electron beam. The process kicks-off with a beam electron exciting the Ti^{4+} cation, ionizing it and creating a vacant site. If the vacancy occurs at the 3p level, then the dominant vacancy-filling process is an inter-atomic Auger process.[17] An electron coming from the valence band of the O^{2-} atoms since there are no electrons available in higher energy levels of the Ti atom. The energy emitted in the core-hole decay is absorbed by one, or two electrons (double Auger process)[18] in the oxygen's valence band which then are ejected as Auger electrons. The aftermath of this process leaves an O$^+$ ion (or a neutral O^0) since it can lose up to three electrons. This process is summarized in Fig. 1.

Prior to this charge sign inversion the O^{2-} anion sits in an attractive Madelung potential created by the surrounding Ti cations. However, once the O anion has been transformed into a positively charged O$^+$ the Madelung potential turns repulsive, as a consequence the ion is encouraged to displace into an interstitial site or to desorb completely if it is near the surface of the specimen. (Neutral O^0 is prone to diffuse through the lattice and eventually get desorbed due to their low reactivity.)

Oxide reduction through the K–F mechanism occurring during in TEM studies is well-documented. In particular, the
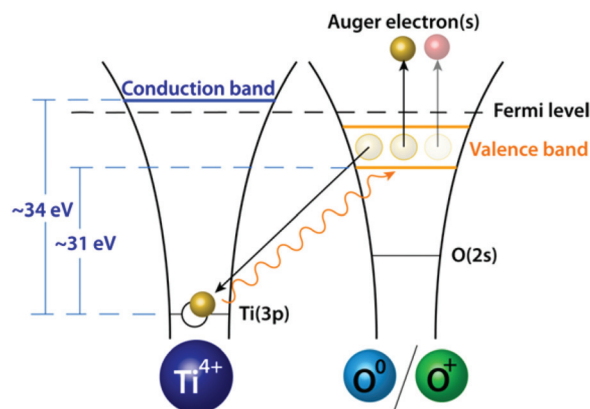

Fig. 1 A photon or around 31 eV is emitted by an electron coming from a O(2p) state filling up a vacancy left in the Ti(3p) state. The photon is subsequently absorbed by one or two electrons from the valence band of the oxygen which then are ejected as Auger electrons. The charge distribution of the TiO$_2$ molecule is drastically changed leaving a positively charged O ion which is then prone to dissociate Sputtering is not the only route leading to material getting desorbed out of an irradiated specimen. The so-called Knotek–Feibelman (K–F) mechanism offers a more indirect pathway to explain the loss of material induced by electron beams without enough energy to provoke sputtering. Surface decomposition and desorption can be observed at beam energies even below 1 keV, far lower than the sputtering energy threshold for any chemical element.

process is especially effective in the case of maximum valency oxides (where the cation and anion are ionized down to their nobel gas configuration) such as SiO_2,[19] Al_2O_3,[20] WO_3[21] and V_2O_5.[22] It has also been suggested that the K–F mechanism can explain the electron beam-induced oxygen desorption in some non-maximum valency oxides such as B_2O_3[23] and MgO.[24]

Specimen charging

Charging effects are of especial importance whenever the specimen under study is an insulating material. Conducting specimens are able to channel away the beam electrons that might get trapped within them. On might speculate that charging in insulating TEM specimens is mainly due to the lack conduction channels to canalize the trapped electrons, however, the charging process is notably more subtle.

The best way to track the charging of a given insulating specimen is to follow the in-flow and out-flow of electrons within the irradiated region. The charge conservation equation through an illuminated region of a typical TEM specimen such as a thin film is:[25]

$$I_0 + I_S = I_T + I_E - I_+ - dQ/dt \qquad (2)$$

On the left hand side we have electron currents entering the irradiated volume while the charges leaving the volume are on the right hand side. I_0 represents the current of the main electron beam, I_S is the electronic current created by the electrons from the regions surrounding the illuminated volume that might flow into it, I_T is the transmitted beam, I_E are the electrons generated by the beam–specimen interactions that manage to escape from the irradiated region, I_+ accounts for ionized nuclei (cations) leaking outwards from the interaction volume and dQ/dt is the change rate of the charge accumulated in the irradiated volume. The currents and charges expressed in eqn (2) are represented pictorially in Fig. 2.

Some sensible assumptions can be made in order to simplify eqn (2). If the material is a good insulator then its valence electrons are not able to move freely within it, then one can assume that $I_S \approx 0$. Moreover, if the film is sufficiently thin then essentially the whole beam is transmitted through, meaning that $I_0 \approx I_T$. Finally, one must take into account that the positively charged ions that make up I_+ are heavy and thus unlikely to diffuse far from their origin spot, thus In consequence, the rate at which charge accumulates within the irradiated volume depends more heavily on I_E, the electrons produced by electron–specimen interactions.

There are mainly three potential processes that are able to produce electrons that contribute to form the stream of I_E. The first of these contributions are the secondary electrons. Secondaries are profusely produced; however, they have low kinetic energies typically falling around the 10 eV mark.[25,26] Thus, a small increase in the (attractive) film potential V_F suffices to effectively cut off the stream of secondary electrons with energies below eV_F.

The second and third contribution can be treated conjointly; these are the currents made of Auger and ejected core
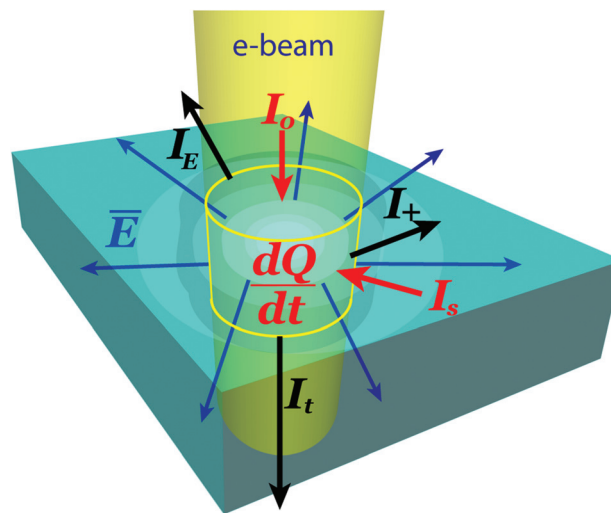
Fig. 2 The terms in red (arrows included) signal the electrical currents flowing into the irradiated volume (yellow cylinder) *i.e.* the beam current I_0, and the electrons flowing in from the surroundings I_S (which in case of an insulating specimen is negligible small) as well as the accumulated charge varying in time dQ/dt. The black terms (and arrows) highlight the electrical currents leaving the specimen, the transmitted beam I_t, the negligible small positive ion leakage I_+ and the emitted electrons produced through beam–specimen interactions I_E which are mainly Auger electrons. An electric field E extends radially outwards and increases its magnitude as dQ/dt grows.

electrons. Both kinds of electrons are energetic enough (hundreds of eV) so as to be able to escape the irradiated volume even after suffering scattering events. However, the effective cross section of the nuclei to be susceptible for Auger emission is considerably larger than that for core electron ionization.[25] For this reason the contribution of core emission pales in comparison to that of Auger electrons. The conclusion is that the charge accumulation rate in the irradiated volume is largely determined by the emitted Auger current.

In a large variety of insulators (such as oxides), Auger electrons are emitted in high numbers just as outlined by the K–F mechanism. It is important to notice that the large Auger current leaving the irradiated volume promotes the accumulation of a net positive charge within it. When this process happens in a reduced volume, such as might be the case when a condensed electron beam probe irradiates a thin TEM specimen, the accumulated positive charge it is highly concentrated. If the beam is condensed down to a probe with a nanometer-sized probe then the irradiated volume looks like a cylinder or a disk depending on the thickness of the specimen. In this construct, the field lines of the electric field associated with this charge distribution extend radially through the specimen pointing outwards with respect to the walls of the irradiated cylinder. As the net accumulated charge grows, the electric field becomes eventually strong enough so as to surpass the dielectric field strength of the specimen itself. After this point the only way for the specimen to recover electrostatic equilibrium is to emit a cascade of positively ionized nuclei that migrate radially away from the irradiated

region.[27] The structure of the specimen is disrupted, the cascade of migrating ions leaves a pit in the irradiated region.

In the case of SEM specimens the charging effect is manifested through an increase of negative charge since SEM specimens are much thicker than TEM. The main cause of charging in SEM specimens is the trapping of secondary electrons that are prevented from escaping into the vacuum.[10] If the specimen is a strong insulator then the trapped secondaries cannot be drained away effectively (even if the specimen is well grounded) and as a consequence there is a growing accumulation of negative charge within the interaction volume. The main difficulty due to this charging is the deflection of the main beam due to electrostatic repulsion at the specimen's surface. The final result will be highly distorted and over-exposed images of the specimen's landscape, which is undesirable during any SEM study.

Electron beam-induced crystallization (phase transition)

The crystallization of amorphous TEM specimens subjected to electron bombardment has been widely documented. Sometimes the crystallization happens locally over small domains of the specimen. At other times and the crystalline domains rapidly extend well beyond the irradiated region; this phenomenon is usually termed "explosive crystallization".

Concerning the explosive crystallization, the broad consensus is that it is a phenomenon triggered by electron-beam heating effects[28–31] despite that it is sometimes acknowledged that the crystallization occurs at a very rapid speed which is uncharacteristic of thermal processes.[29] However, this type of phenomenon cannot be controlled to produce well-defined nanostructures do to the explosive nature of the process.

There is more disagreement about the physical causes behind the formation of small crystalline domains on samples irradiated by an electron beam probe. Some arguments on favor of beam heating-induced crystallization have been put forward for irradiated oxide films oxides[32–37] and possibly for Zr films.[38] On the other hand, observations advocating for an a-thermal crystallization process of thin films are more numerous.[38–49]

The driving mechanisms behind the (re)crystallization processes in most cases can be subdivided in two categories depending on whether the energy of the main beam E_0 is large enough to overcome the displacement energy E_d of the irradiated material. If the E_d threshold can be reached, then, the crystallization is attributed to the creation/recombination of point defects and enhanced atomic mobility. In principle, highly energetic electrons are necessary to drive the crystallization through these elastic processes.[40,41,47,48]

If E_d cannot be reached, then the crystallization mechanism relies on the breaking of "incorrectly" formed a–c interfacial bonds which then reconstitute in a crystalline configurations.[38,39,42,44,45,49] The E_d threshold is lowered at defective sites so that the crystallization process can by driven by elastic energy transfer events.[43]

Qin and collaborators provided a more detailed mechanism to explain athermal beam-induced crystallization.[50,51] The
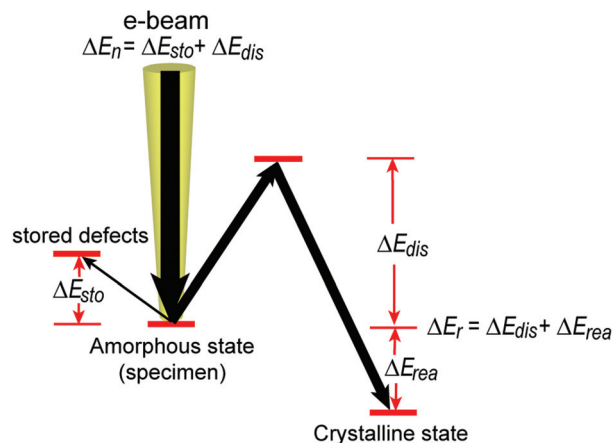
Fig. 3 Schematic representation of the redistribution of the incoming beam energy along an irradiated amorphous specimen according to Qin et al.[51] Most of the energy input is used to excite the atoms of the specimen and only a small fraction gets stored in the form of defects. The atoms in stimulated specimen rearrange until they adopt a crystalline configuration as the specimen decays into a lower energy state (lower than the original amorphous state).

crystallization pathway explains how an amorphous disordered atomic structure (relatively high internal energy) can lower its internal energy to end up in a crystalline (highly ordered) even when it is subjected to the constant energy input supplied by the e-beam (seen schematically in Fig. 3). The energy injected by the beam ΔE_n is redistributed into two parts, a fraction is stored in the form of generated defects ΔE_{sto} that contribute to the atomic disorder of the specimen. Another fraction is dissipated into the environment ΔE_{dis} as the impacted specimen's atoms rearrange in order to relax the atomic structure. During the rearrangement process the specimen is driven to a "stimulated state" which is thermodynamically unstable and quickly decays releasing a total amount of energy ΔE_r. After the rearrangement is completed the internal energy of the specimen drops a factor ΔE_{rea} below to the energy value of the initial amorphous state. ΔE_{rea} accounts exclusively for the differences in free-energy of the post-rearrangement crystalline configuration with respect to the initial disordered state. The likelihood of the specimen landing on a crystalline phase as it rolls down the internal energy landscape is high since typically such configurations occupy the deepest energy valleys.

Electron beam induced synthesis of quasi zero-dimensional nanostructures

Nanoparticles

Two main approaches dominate the protocols for the e-beam-induced synthesis of nanoparticles: the electron beam induced fragmentation (EBIF) of a precursor and the local beam-induced nucleation/precipitation of crystalline nanoparticles that embedded in thin films. It is largely agreed that EBIF reac-

tions are driven by beam-induced heating aided in some cases by charging effects.[52,53] On the other hand the beam induced crystallization processes are thought to be driven by athermal processes.[50,51,54] First, the literature dealing with the synthesis of nanoparticles through EBIF is reviewed.

EBIF synthesis of nanoparticles

In EBIF a micrometer-sized precursor is irradiated by a gradually converging electron beam. In a typical experiment the electron beam of the TEM is gradually condensed over a precursor particle. As the current density increases the precursor might suffer structural transformations (shape changes, volume loss) until after a certain current density threshold it undergoes an "explosive" reaction in which large numbers of nanoparticles are ejected outwards (fragmentation). The nanoparticles are caught by the carbon support of the TEM grid. The largest nanoparticles lie closer to the precursor particle and their size gradually decreases as their distance from it increases. In some cases, the nanoparticles gradually gain size if the fragmented precursor continues to be irradiated by a convergent beam.

Nanoparticles made of a large variety of materials have been produced through EBIF. Most of the EBIF experiments have been directed towards the production of metallic nanoparticles made out of a single element. Herley and Jones[55] pioneered the field reporting the production of various metallic nanoparticles (Ti, Mn, Ni, Ag, Sn, Fe, Bi, Co, Cd, Sb, La, Ce and Ti) by fragmenting micron-sized precursors made of their respective azides with the general formula MN_3. The precursor particles melt and collapse into spherical beads as the irradiating current density increases (up to around 10 A cm^{-2}). During the process, the metallic nanoparticles are expelled and can fly up to 10 microns away from the precursor azide. The authors argue that the EBIF mechanism relies on beam-induced heating since there is an "approximate correlation" between the energy flux needed to drive the EBIF reaction and the melting points of the precursors. The authors do not elaborate about the kind of radiolysis reaction that decomposes the azide precursor into purely metallic nanoparticles and (presumably) nitrogen gas. This investigation set the stage for further experiments. It established the outline for a standardized EBIF protocol and also set the interpretation of EBIF reactions as mainly thermally-driven phenomena.

Confirmation of the critical role of beam-induced heating in EBIF reactions came 17 years after this seminal work. Caldwell et al.[53] performed cathodoluminescence (CL) spectroscopy on semiconducting GaN nanowires as they fragmented under a convergent beam. The authors calculated the temperature increment on the nanowires by analyzing the CL spectra. The photons emitted by a heated nanowire have a lower frequency (lower energy) with respect to those emitted by "cold" nanowires since the bandgap of GaN closes due to thermal effects such as photon–phonon interactions and crystalline lattice dilation.[56] Applying the model of O'Donnell and Chen to calculate the bandgap shift due to thermal effects,[57] Caldwell et al. estimate that the observed bandgap closing can be attrib-

uted to a temperature rise of 1200 K, sufficient to melt the nanowires and cause an "explosive" reaction. Nevertheless, it is interesting to notice that an alternative explanation for the bandgap in the CL spectra could alternatively be given in terms of the generation of an internal electric field produced by trapped electrons and superficial charging.

Q. Ru incorporated the hypothesis that charging effects might contribute significantly at driving the fragmentation process, a possibility that was not considered by Caldwell et al. Ru obtained large yields of Au nanoparticles by fragmenting porous micron-sized Au beads with electron beam pulses delivered inside a TEM.[58] (The energy of the electron beam was 200 kV and the current density reached 10 kA cm^{-2}.) The crucial observation was that less porous Au beads were less prone to fragmentation. Ru then concludes that besides beam-induced heating, charges can accumulate within the pores giving rise to a repulsive Coulomb force. The repulsive forces build up rapidly and work alongside heating effects to instigate the fragmentation of the precursor.

In subsequent works, the list of mechanisms assisting EBIF reactions was enlarged. Beam-induced heating retained its leading role at driving fragmentation reactions followed closely by charging effects. In particular, the latter processes are called in to explain the subsequent growth of the expelled nanoparticles as the precursor continues to be irradiated after the initial fragmentation has taken place.

Some works rely almost exclusively on thermal effects to explain the EBIF processes they describe. Beam-induced heating explains the decomposition of LiF crystals into Li nanoparticles that continue to grow and morph as the crystals were irradiated by a condensed beam after fragmentation has occurred.[59] NiO/ZrO_2–CeO_2 and NiO precursors decompose thermally under convergent electron irradiation to produce Ni nanoparticles (although the authors point out that the presence of environmental CO coming from the diffusion pump might mediate the reduction reaction triggered by the e-beam).[60] The Ni nanoparticles grow larger due to sintering driven by thermally enhanced mobility of Ni atoms as the precursor keeps on being irradiated. Lu et al. produced Fe-doped orthorhombic SnO_2 nanoparticles out of a tetragonal (rutile) SnO_2 lump with a 5% molar concentration of Fe.[61] The authors explain that beam-induced heating drives a phase transition of the precursor particles. As heat builds up within the precursor there is rise of its internal pressure that promotes rutile-to-tetragonal phase transition. Ultimately the growing pressure causes the external layers of the precursor to get ejected thus completing the fragmentation reaction.

Heating and charging acting coordinately are suggested to explain several EBIF experiments. The fragmentation of Pb particles covered with a thin oxide layer into Pb nanoparticles is explained in terms of both effects acting simultaneously.[62] Pyrz et al. produced bimetallic Bi–Ni nanoparticles by instigating EBIF on micron-sized particles containing Bi and Ni in different proportions (see Fig. 4c and d).[52,63] The authors reason that the fragmentation starts by incongruent melting of the Bi phase (lower melting point) leading to the formation of
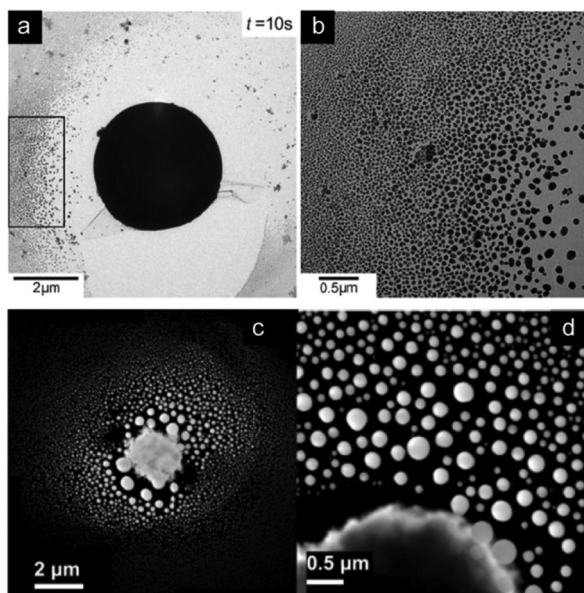
Fig. 4 (a) Fragmented Ag microparticle after being exposed to a convergent electron beam for 10 seconds. Panels (b) shows a magnified view of the region enclosed within a back rectangle in panel (a) where the individual Ag nanoparticles ejected after the EBIF reaction can be clearly discerned. The reduction in nanoparticle size as a function of the distance to the precursor is evident here. (c) and d) are high-angle annular dark field images of a Bi–Ni microparticle precursor and the bimetallic Bi–Ni nanoparticles lying around it after the EBIF reaction has taken place. The individuality of the nanoparticles is attributed to repulsive forces due to superficially accumulated charges. Panels (a) and (b) reproduced with permission from ref. 66. Copyright 2010 Springer. Panel (E) reproduced with permission from ref. 52. Copyright 2007 American Chemical Society.

liquid pockets. The interstitial liquid is more susceptible to accumulate charge creating large repulsive forces within the precursor. Thus, beam-induced melting and charging lead the fragmentation. In favor of this hypothesis the authors noted that the precursors are more prone to fragment if the Bi content is as high as 75%. They also point out that the nanoparticles keep their individuality instead of coalescing due to superficial charges being retained from the fragmentation reaction. Buck et al. produced GeTe cubic nanocrystals out of fragmented GeTe microcrystals.[64] The authors explain the fragmentation reaction along the same lines sketched by Pyrz et al. i.e. incongruent melting of the Te phase followed by charging of the liquid phase.

The hypothetical relevance of sputtering, atomic displacement, and radiolysis processes in EBIF has been highlighted in at least one work. Gnanavel et al.[65] explain the growth of Co nanoparticles of different morphologies expelled from the fragmentation of hydrated CoF_2 particles as a consequence of sputtering and enhanced atomic mobility due to knock-on collisions between electrons and the precursor atoms.

Sublimation or sputtering is thought to be a relevant mechanism for the growth of the Co nanoparticles at the highest current density employed by the experimenters. Li and Zhang

produced fields of Ag nanoparticles by irradiating Ag microparticles with a convergent e-beam (see Fig. 4a and b).[66] Here the authors refer to the Ag nanoparticles produced through the EBIF process as being "sputtered away" from the precursor Ag microparticle. If the microparticle is further subjected to irradiation then the size of the Ag nanoparticles increases, presumably though continuous sputtering of Ag atoms.

The work of Yen et al. on the EBIF of Cu nanoparticles by exposing CuCl precursors to a convergent e-beam limits itself to describe the evolution of the phenomenon without delving on the physical causes that might be behind it.[67]

Nucleation/precipitation of nanoparticles induced by electron beam irradiation

The gradual and controlled nanoparticle nucleation and growth under electron beam irradiation is a well explored research field. Scores of materials susceptible to the formation of beam-induced crystalline domains that evolve into what can be labeled as a nanoparticle have been reported. The precursor materials (substrates) are in most cases thin amorphous-glassy films or ribbons but they can also be polymers, layered substrates and micron-sized particles.

In many cases, the nanoparticles formation follows a two-step process. The first step involves beam-induced decomposition of the chemical structure of the substrate. This can happen through a radiolytic process or through phase separation induced by heating. The precise radiolytic pathway varies from one case to another depending on the initial chemical composition of the substrate. The second step consists on atomic re-arrangement happening in the small domains that were previously chemically modified. The re-arrangement is promoted by events such as atomic displacements through knock-on collisions or even charging effects. Cases of nanoparticles precipitation following this general two-step framework described are presented next.

In many of the cases, the substrates are amorphous films that act as matrices for the beam-produced crystalline nanoparticles. Du et al.[68] promoted the formation of crystalline Si nanodots embedded within an amorphous SiO_2 (a-SiO_2) film. The first step of the process involves beam-induced reduction of the (a-SiO_2) film transforming it into an amorphous Si (a-Si) substrate. The decomposition is thought to happen through the K–F mechanism. Gradually, Si–O bonds are replaced by Si–Si bonds in an amorphous configuration forming nanometer-sized a-Si domains throughout the substrate. Finally, the a-Si domains crystallize into crystalline nanodots mainly through knock-on displacements.

Zn nanoparticles have been precipitated by irradiating a variety of substrates such as amorphous $Zn_{2x}Si_{1-x}O_2$ films,[69] glassy $ZnO–B_2O_3–SiO_2$ (see Fig. 5a–d),[70] $Zn–B_2O_3–SiO_2$ and $ZnO–Na_2O–B_2O_3–SiO_2$ glasses.[71] A highly focused beam is used throughout all these protocols, this allows for high spatial control over the locations where the nanoparticles are to be precipitated. All these cases follow essentially the same rationale based on a two-step process. Zn ions are produced through radiolysis processes in a kind of "variation" of the K–F
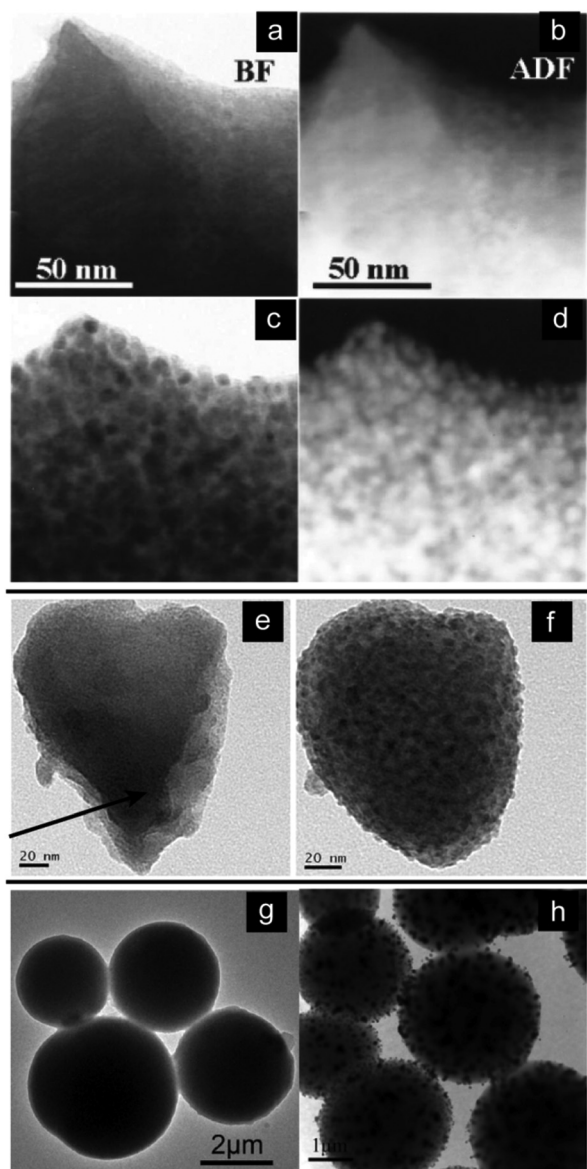
Fig. 5 (a) and (b) Bright field image and (c) and (d) annular dark field images of an irradiated piece ZnO–B$_2$O$_3$–SiO$_2$ glass. (a) and (b) Were taken after 0.1 ms of exposure while (c) and (d) were obtained after 1 s of exposure. The densely packed Zn nanoparticles can be clearly discerned in (c) and (d). (e) Bismuth-based glassy particle in its initial state and (f) after 2 minutes of e-beam irradiation. Vast amounts of Bi nanoparticles nucleate within the glassy precursor particle. (g) Shows a carbonaceous particle with cupper species before being exposed to a convergent electron beam. (h) Copper nanoparticles nucleate and rapidly move towards the precursor's edges as the beam is condensed over the carbonaceous precursors. Panels (a)–(d) reproduced with permission from ref. 70. Copyright American Institute of Physics 2000. Panel (e) and (f) reproduced with permission from ref. 74. Copyright Springer 2011. Panels (g) and (h) reproduced with permission from ref. 80. Copyright Elsevier 2014. That a thermal mechanism driven by beam-induced heating might be at play.[74]

mechanism compared to that experienced in most of the irradiated oxides (the initial core-holes are created in the O$_{2s}$ levels rather than in the metallic cation). Afterwards the Zn

ions migrate due to built-in electric fields and are subsequently neutralized through the capture of Auger. The final product is a crystalline Zn nanoparticle formed within the small irradiated volume.

There is a good share of research dedicated to the *in situ* production of embedded bismuth nanoparticles. Bi NPs have been obtained from commercially available NaBiO$_3$ microparticles.[72]

Although the authors explicitly state that the formation process is not fully understood they hint towards a two-step process. First, the NaBiO$_3$ precursor decomposes radiolytically producing Bi^{5+} ions and neutral Bi^0 that segregate and nucleate into small crystalline seeds (O and Na might get volatilized in the process). The seeds then coalesce into larger nanoparticles *via* Ostwald ripening processes driven by beam enhanced diffusion, (possibly by knock-on collisions). Other reports about *in situ* produced Bi nanoparticles are somewhat vaguer about the formation process. Kim *et al.* produced Bi nanoparticles by irradiating BiCl$_3$ films. The authors limit themselves to state that the growth of the nanoparticles is due to beam-enhanced atomic diffusion.[73] Bi NPs can also be produced by irradiating micron-sized pieces of bismuth-based glasses (see Fig. 5e and f). The authors of this work do not fully tackle the issue of the growth process, however, they point out that the low melting point of Bi might facilitate the process. This seems suggest.

Several kinds of nanoparticles can be produced by irradiating metallo–organic frameworks (MOFs) filled with the desired precursor. However, here most of the synthesis procedures depart from the common two-step processes (decomposition + atomic rearrangement) outlined before. Of all the reports on *in situ* nanoparticle production in MOFs, only that from Kim *et al.* can still be easily classified into this category.[75] The researchers produced monodisperse Au nanoparticles through the beam-induced decomposition of a gold containing polymer (Au(ɪ)–SC$_{18}$). After decomposition, Au atoms diffuse and nucleate into nanoparticles. The phenomenology rest of the works presented in this subsection does not conform with the two-step scheme described above, thus, it is better to treat each case separately.

The synthesis of Ag nanoparticles by irradiating various MOFs proceeds through a different route.[76,77] Houk, Jacobs and coworkers selected a variety of crystalline MOFs with different pore sizes for their studies. The pores were then infiltrated and filled with aqueous AgNO$_3$. The nanoparticle nucleation process is somewhat more complex in these experiments. The authors describe that the MOF rapidly decomposes under the beam irradiation. Ag$^+$ ions were present in the AgNO$_3$ solution right from the loading procedure. Thus, when the beam destructs the physico-chemical barriers imposed by the MOF scaffold, Ag clusters are free to form and nucleate into nanoparticles. An analogous procedure can be extended to Cu and ZnO-based MOFs.[78]

Díaz *et al.* produced crystalline SiP$_2$O$_7$ nanoparticles by bombarding a pyrolitic organo–metallic derivative of cyclophosphazenes.[79] The precursor is loaded with pyrolitic phospha-

zene and SiO_2 byproducts stabilized by a scaffold made of amorphous P_2O_7. When irradiated, beam-induced heating drives a reaction between the byproducts and the supporting scaffold yielding crystalline SiP_2O_7 nanoparticles separated by amorphous walls of unconsumed P_2O_7. Perhaps the most advantageous feature of the production of nanoparticles supported by a MOF structure is that their size is easily tunable by controlling the pore size of the scaffold.

Pure beam-induced heating has also been purported as the driving mechanism for the *in situ* production of Cu NPs. The nanoparticles were obtained by irradiating micron-sized carbonaceous microparticles containing Cu species (see Fig. 5g and h).[80] The initially smooth microspheres transform rapidly under the action of the converging beam (protocol similar to EBIF). Cu nanocrystals form and are projected towards the surface of the. The authors suggest that the beam elevates the composite's temperature thus accelerating the diffusion of Cu, forming clusters that migrate rapidly towards the precursor's edges.

Athermal accounts of the beam-induced nanoparticle precipitation can also be found. Xie and coworkers[81] produced monoclinic CuZr NPs by irradiating $Cu_{50}Zr_{45}Ti_5$ glassy samples. Here the synthesis process also does not quite fit the two-step scheme provided before. No radiolysis process is invoked; instead, the growth proceeds solely through a type of selectively enhanced atomic diffusion mechanism. The authors argue that an almost fluid motion of the CuZr phase can be attained by athermal means; instead they allude to continuous electron-nuclei collisions, the creation of vacancies and interstitials as the mechanisms enhancing atomic diffusion. The CuZr phase precipitates into nanoparticles that remain stable under the beam illumination.

The electron beam of the TEM can also drive chemical reactions between the surface of a substrate and the small amounts of gases present in the observation column in order to produce nanoparticles. Su *et al.* produced In_2O_3 nanoparticles sitting over the surface of In_2S_3 nanosheets as they were irradiated by in the TEM.[82] The nanoparticles grow gradually at the edges of the polycrystalline nanosheets. Until the nanosheets themselves transform into clusters of partially coalesced nanoparticles. The authors propose that the growth process is initiated when the beam distorts the bonds of the In_2S_3 nanosheets forming interstitials and dangling bonds. Gradual oxidation takes place as the dangling bonds react with residual O and water vapor of the TEM column thus producing the In_2O_3 NPs.

Yet another different approach based on pressure building up due to knock-on damage has been implemented to MgO clusters out of MgO films covered by a thin Au layer.[83] The growth process is initiated at Au nanoparticle protrusions sitting on short MgO rectangular monticules at the edges of the MgO film. Upon increasing the current density the Au NP gets pressed into its rectangular MgO support. The pressure needed for the Au NP insertion into the subsrrate is suggested to occur as a consequence of the force exerted by knock-on processes between the beam electrons and individual Au atoms of the NP. As the Au NP nests into the MgO support it mechanically cleaves an individual MgO cluster that is subsequently transported to the top of the Au NP. If the current density is decreased the Au NP is pushed back outwards as the force acting upon it is reduced.

There is at least one report of *in situ* nanoparticle synthesis inside a SEM. Kojima and Kato[84] fabricated Au nanoparticles dispersed over large plain areas by irradiating a thin Au layer (5–30 nm) deposited over a Si/SiO_2 substrate. Furthermore, they could produce patterned arrangements of Au NPs by irradiating Au layers deposited over periodically holed Si/SiO_2 substrates. The fields of nanoparticles are generated by a dewetting process of the uniform Au layers. The rupturing of the film is caused by a sharp thermal gradient generated on the superficial layer due to electron beam heating. A surface tension gradient is generated on the molten Au layer which locally regroups forming the Au NPs.

Other kinds of quasi-zero dimensional nanostructures

There are quasi-zero dimensional nanostructures other than solid-core nanoparticles that can be obtained through *in situ* beam-induced synthesis methods. For instance, one can produce nanostructures consisting on cages with atom-thick shells that are denominated as fullerenes when they are made of carbon and $B_{12}N_{12}$ cages (the BN analogue to C fullerenes). When further layers envelope a central fullerene (or its boron nitride equivalent) one gets concentrically layered structures that are referred to as nano-onions.

Multilayered nano-onions, first made of carbon and then of boron oxide, were produced by electron beam irradiation before fullerenes and $B_{12}N_{12}$ cages could be achieved. This is not surprising since the precursors needed for the *in situ* beam-induced production of the latter are notably harder to prepare. Nano-onions can be obtained by irradiating bulkier soot-like materials that are relatively easy to obtain while fullerenes and single-shell BN cages need higher quality precursors like graphene (an atomically thin sheet of C) and regularly layered BN substrates.

The driving mechanisms proposed for the synthesis of C nano-onions have "evolved" over time. In a sense, one could say that they converged towards the main mechanism responsible for the production of C and BN fullerenes, *i.e.* strain induced by knock-on damage (sputtering) of the layered precursor materials. Initially beam-induced heating was proposed as the leading mechanism for the production of nano-onions.[85] However, subsequent works gradually put more emphasis on the structural relaxation that follows after the removal or displacement of atoms by knock-on collisions. Pure carbon nano-onions were first produced by bombarding graphitic needle-like particles (carbon soot) with electrons were first obtained in 1992 by D. Ugarte (see Fig. 6a–c).[85] The author considers that the nano-onions formation is instigated by electron beam annealing. The process is initiated by the simultaneous collapse of the graphitic needles into spherical particles and their epitaxial graphitization due to beam-induced annealing. Microscopically, the heat pumped in by
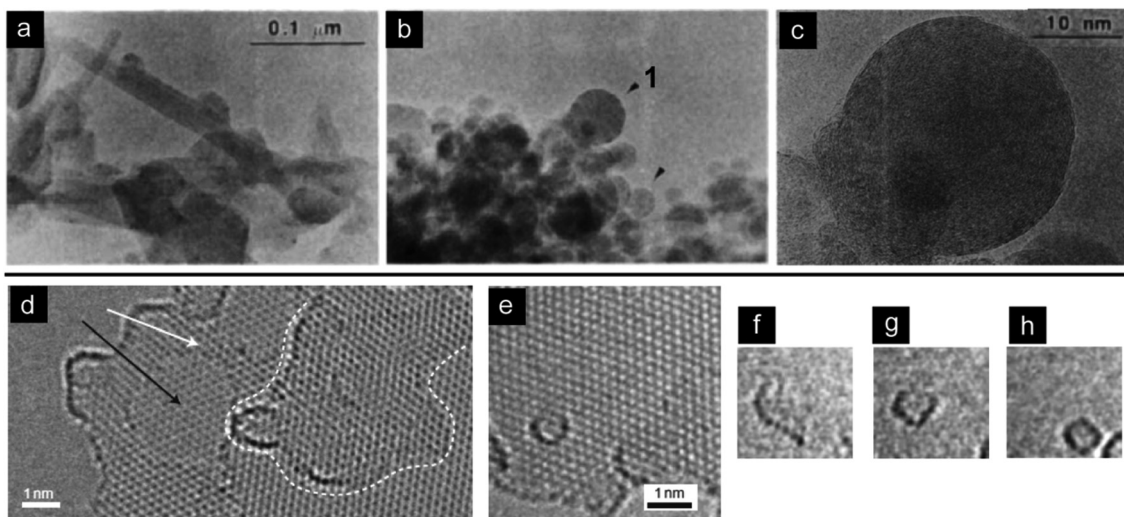
Fig. 6 (a) Graphitic needles found in carbon soot material. (b) The needles transform into closed spherical carbon nano-onions after 20 minutes of irradiation with a 300 kV e-beam. (c) High magnification image of the onion marked with the arrow "1" in (b). The multiple concentric graphitic layers of the nano-onion can be appreciated. (d) Few layer graphene substrate utilized for the beam-induced synthesis of fullerenes. The black arrow indicates a bilayer of graphene upon which a strip of single layer marked with the white arrow is deposited. (e) Overview of a fullerene sitting of a graphene substrate. The fullerene is obtained after the deposited flakes curl and zip up completely. Some screenshots of the curl-up process can be appreciated from panel (f) to panel (h) where the fully closed fullerene has been produced. Panels (a)–(c) reproduced with permission from ref. 85. Copyright Nature Publishing Group 1992. Panels (C) and (D) adapted with permission from ref. 93. Copyright McMillan Publishers Limited 2010.

the electron beam produced dangling bonds that rearrange themselves in order to minimize the energy of the structure. This is attained by forming concentric graphitic spheres, *i.e.* graphitic nano-onions. Lulli *et al.* essentially reproduced Ugarte's experiment by bombarding graphitized carbon particles with electrons.[86] The authors performed systematic studies at different acceleration voltages and current densities that lead them to conclude that there is a threshold value for both parameters in order to drive the synthesis to completion: from 100 to 150 kV for the voltage and a current density of around 150 A cm^{-2}. The voltage threshold highlights the importance of atomic displacement and defect creation in the formation mechanism, while, the current density threshold could be interpreted either as the relevance of an increase in beam-induced heating or an increase in the rate of atomic displacement events. Zwanger *et al.* ruled out the effect of beam-heating during the formation of C nano-onions by irradiating carbon soot, carbon films, amorphous C deposits and crystalline graphite at various voltages inside a pair of TEMs.[87] The authors observe that the nano-onion formation is enhanced at higher voltages while the dose threshold necessary to trigger the process actually decreases with increasing the accelerating voltage. If heating effects were the leading mechanism this trend should be reversed. Thus, the authors conclude that "displacement cascades" triggered by electron-nuclei collisions are the main formation mechanism (the maximum employed voltage was of 1250 kV, where the nano-onion formation is enhanced and most of the collisions result in atomic displacements). Ru *et al.* speculated that magnetic forces building up within the shells of the nano-onions.[88] The kinetic energy of the π electrons on the pentagonal rings of the graphitic layers

is increased by collisions with beam electrons; this creates paramagnetic ring currents that exert a force upon the whole structure by generating a magnetic field. The role of the force is mainly to align the nano-onion with respect to the electron beam while it continues to grow.

Electron beams can also trigger the growth of C nano-onions in the presence of metals that catalyze the formation process. In fact, some of the metallic material can get trapped within the graphitic layers rendering hybrid structures with metallic atoms intercalated between the graphitic layers. In general, the catalytic role of the metals is to accelerate the process by facilitating the rupture of C–C bonds by directly transferring some of the energy absorbed from the main beam. This approach was taken by Oku *et al.* while producing C nano-onions by irradiating amorphous C with Pd clusters.[89,90] In another work "giant" carbon onions (up to 37.5 nm in diameter) were produced by irradiating Al nanoparticles sitting on an amorphous C film.[91] The onions initiate their growth at the Al/C film interface while the beam is simultaneously illuminating a group of nanoparticles sparsely distributed over the film. The general catalytic scheme is followed here: the energy of sputtered C atoms is further increased by energy being transferred to them from ionized Al resulting in the breaking of amorphous C–C bonds and leading to graphitization (some Al atoms are intercalated between the graphitic layers in the process). Remarkably, onions near the edges of the irradiated region reach a maximum radius. Troiani *et al.* observed fullerenes growing at an "explosive rate" over the surface of irradiated Au and Au/Pd nanoparticles sitting over a thin C film deposited over a TEM grid.[92] Nano-onions with between 9 and 10 layers are formed after only 2 minutes of

irradiation. The shape of catalytic nanoparticles constantly fluctuates as they are being irradiated. It is thought that this fluctuation increases the catalytic activity of the nanoparticle. As in the previous cases, the process is set into motion by atomic displacements provoked by electron-nuclei impacts.

Chuvilin et al. achieved the production of single-shell C fullerenes for the first time by irradiating pristine graphene sheets (see Fig. 6d–h).[93] The fullerene formation follows a two-step process. In the first step small graphene flakes are fragmented from the graphene's edges by knock-on damage. The flakes are then adsorbed on top of the graphene sheet. In the second step the flake's lattice is distorted by sputtering: pentagonal rings are formed due to the loss of C atoms. The flake curls up by stresses associated with the gradual proliferation of pentagonal rings are until it is able to zip up forming a completely closed fullerene. As stated before, BN nano-onions have been produced in at least three different occasions by electron beam irradiation. The first attempt by Banhart et al. could only produce BN onions while irradiating amorphous BN with a 1250 kV e-beam.[94] The synthesis process lasted for at least 75 minutes and only succeeded at producing unstable BN onions. The nano-onions are formed by atomic "displacement cascades" just as in the case reported by Zwanger et al. during the formation of C nano-onions.[87] Closure cannot take place since dangling bonds cannot be completely saturated. This is thought to be a consequence of the nano-onions the arrangement of B and N atoms in the BN layers and geometrical considerations (pentagonal rings cannot be formed as in the case of C because that would require B–B or N–N bonds which are not energetically favorable). However, Stèphan et al.[95] and Goldberg et al.[96] succeeded at producing $B_{12}N_{12}$ cages (BN fullerenes) by irradiating turbostatic layered BN (b-tBN) and multi-walled BN nanotubes (BNNTs) in the first work and hexagonal

BN in the second work. The layered nature of these precursors is essential to successfully synthesize closed BN cages. The layers are joined together by relatively weak van der Waals forces which facilitates their "peeling off" when they are bombarded with energetic electrons. Multilayered onions are peeled off from the b-tBN, the authors consider that the layers might curl up due to superficial charge accumulation and that no loss of matter occurs in this case. On the other hand, single-shell $B_{12}N_{12}$ cages can be obtained by irradiating either the multi-layered BNNTs or the hexagonal BN flakes. Here the authors speculate that sputtering drives the curling up process. Strain is created by the removal of atoms until a structure made of alternating B–N bonds forming square rings separated by hexagonal rings corresponding to the smallest stable closed $B_{12}N_{12}$ molecule is obtained.

Nanoparticles/nanowires hybrids

At times, the solid precursor used to instigate the growth of nanoparticles is itself a nanostructure instead of a larger scale material. In particular, one-dimensional nanostructures such as nanowires can be used as precursor materials for the beam-induced synthesis of nanoparticles. The end product of such a process is a sort of hybrid nanostructure combining nanoparticles distributed over a one-dimensional substrate. Three works are presented in this section and the synthesis process in each of them differs significantly from one another, thus, they will be treated separately.

Ramasamy et al. irradiated dipeptide nanotubes covered by Au_{25} quantum clusters and protected by a gluthathione (GSH) layer (see Fig. 7e).[97] The clusters are attached on both of the nanotube's surfaces, inner and outer. The irradiation causes
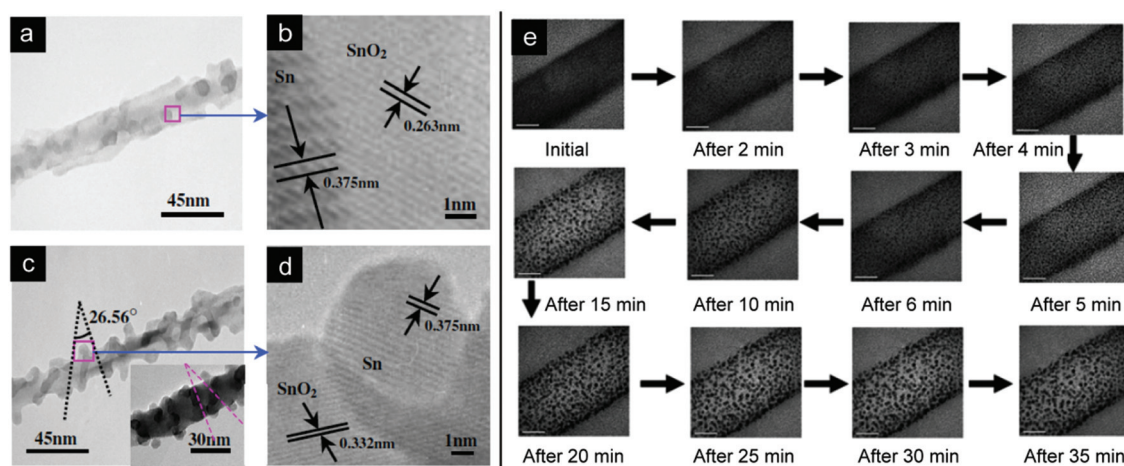
Fig. 7 (a) Onset of the formation of Sn−SnO₂ nanopeapods (Sn nanoparticles contained within SnO₂ nanotubes) out of coaxial Sn−SnO₂ nanowires exposed to 200 kV electron irradiation. (b) High magnification image of the boundary between and Sn NP and SnO₂ nanotube. (c) After a second irradiation stage the Sn NPs are ejected outside the SnO₂ shell and enwound the SnO₂ nanotubes. (d) High magnification image of an extruded Sn NP. (e) Sequence of images of the nucleation and growth of Au NPs anchored on a dipeptide nanotube as the electron irradiation time increases (scale bar: 20 nm). Panels (a)−(d) reproduced with permission from ref. 98. Copyright Institute of Physics publishing all rights reserved 2006. Panel (e) adapted with permission from 97 Copyright The Royal Society of Chemistry 2009.

the 0.7 nm clusters to aggregate and coalesce into 4 nm wide Au nanoparticles, thus, the end product is a dipeptide nanotube decorated with Au nanoparticles attached on both of its surfaces. The authors explain that the Au_{25} clusters are inherently unstable but the GSH layer and the curved surface of the nanotubes provide them with stability. However, that stability is disrupted by the bombarding electrons to the point in which the clusters are allowed to coalesce, presumably by partially destroying the GSH coating.

Wang *et al.* irradiated coaxial Sn–SnO_2 nanowires transforming them into SnO_2 nanotubes decorated with Sn nanoislands (see Fig. 7a–d).[98] The transition has an intermediate step in which the nanowires turn into so-called nanopeapods: SnO_2 nanotubes containing a string of Sn nanoparticles. The authors calculate that the temperature rises to 439.9 °C in the nanowire (the current density is of 10 A cm^{-2}) which is higher than the melting point of Sn (231.9 °C), thus, the fragmenting of the Sn core and its further coalescence into nanoparticles is driven by beam-induced heating. A certain amount of the SnO_2 shell is lost during this process due to radiolytic processes. In the final step the Sn nanoparticles protrude outwards filtering through the SnO_2 shell in a process referred to as "nano-jet". The process is driven by the pressure exerted by the dilating Sn nanoparticles against the SnO_2 walls. The expansion of the NPs is thermally driven. The process continues until small Sn islands fully traverse the walls and align into a chiral arrangement that enwinds the SnO_2 nanotubes.

Finally, Zhang *et al.* produced CuO nanowires decorated with Cu_2O nanoparticles by irradiating micron-sized Cu_2O remnants attached to the nanowires with a convergent e-beam.[99] Typically, a single Cu_2O microparticle hangs from a "clean" CuO nanowire. The morphology of the Cu_2O microparticle changes as it is irradiated by the condensed beam, simultaneously, small Cu_2O commence to appear regions of the nanowire that can be as far as 5.5. μm away from the Cu_2O microparticle. Mass has been transferred from the Cu_2O cluster to the surface of the nanowire, however, the authors offer no physical explanation behind this mass transfer process.

One-dimensional nanostructures

Catalyst-assisted beam-induced synthesis of nanowires

To our knowledge there is only one report of beam-induced catalyst-assisted growth of nanowires. This is because of the inherent difficulties of implementing the experimental conditions needed to achieve growth *via* the VLS or VSS mechanisms (the most common catalyst-assisted growth mechanisms) inside the TEM column. Such experiments essentially consist on reproducing the conditions of a CVD setup inside the TEM column, a task that requires either a TEM with environmental capabilities ETEM or specimen holders with heating capabilities (or both) since both mechanisms necessitate temperatures well above room temperature to activate the catalyst reactions. This issue is a major obstacle

for coming up with synthesis protocols to instigate the catalyst-assisted growth since the only way to achieve significant heating with an electron beam is to condense it into a small probe and increase the total current as much as possible. However the temperature only rises over the irradiated region and its close vicinity, instead of elevating the temperature of the whole specimen and its surroundings.

Gonzalez-Martinez *et al.*[100] produced amorphous core–shell B/BO_X NWs and BO_X nanotubes by irradiating a composite microparticles made of Au nanoparticles embedded within an amorphous B_2O_3 matrix. The composite is irradiating by an increasingly converging beam. After a certain current density threshold the Au NPs move towards the precursor edges protruding outwards from the B_2O_3 matrix. Nanowires grow from the protruding Au nanoparticles extending in all directions as the precursor is irradiated by the condensed e-beam. The role of the convergent beam is to generate feedstock material by disrupting the precursor's structure through electron beam charging (the process is explained in section 2.3). Cascades of B^+ ions alongside oxygen vapors are generated within the irradiated volume through charging and radiolysis by the K–F mechanism. The feedstock B ions then travel from the irradiated volume until the reaction sites in the Au NPs at the tips of the nanowires. The transport of feedstock material is instigated by the radial electric field associated with the charging process. The solid Au nanoparticles become catalytically active in the presence of the O_2 vapors that are generated alongside the feedstock material.[101] The growth of the nanowires can proceed for as long as there is enough B to be turned into feedstock material within the irradiated region (see Fig. 8a). Small amounts of oxygen can still be desorbed as the precursor becomes boron depleted. The oxygen keeps the Au nanoparticles active, however, in the absence of feedstock they react with the B core of the nanowires. The reaction volatilizes the B core leaving only the BO_X shell intact. The length of the BO_X left behind the catalytic Au NPs extends as they move towards the nanowires bases volatilizing the B cores along their way. Gradually, the nanowires are therefore turned into BO_X nanotubes (see Fig. 8b).

Catalyst-free beam-induced synthesis of quasi-one dimensional nanostructures

Reports describing the production of nanowires inside the TEM without the need of a catalyst material are more numerous. One can classify the experiments according to three main synthesis procedures: (1) growth by extrusion, where the nanowires grow rooted at their base to the precursor material. (2) Growth by fragmentation. A procedure similar to EBIF. (3) Growth by global morphological transformations, where large sections of (or the whole) the precursor material transform into bundles of nanowires. Each of these modes has its own set of characteristic physical processes driving the growth mechanisms. Let us start with examples of growth by extrusion.

Growth by extrusion requires the generation of a force field within the precursor materials in order to drive the precursor
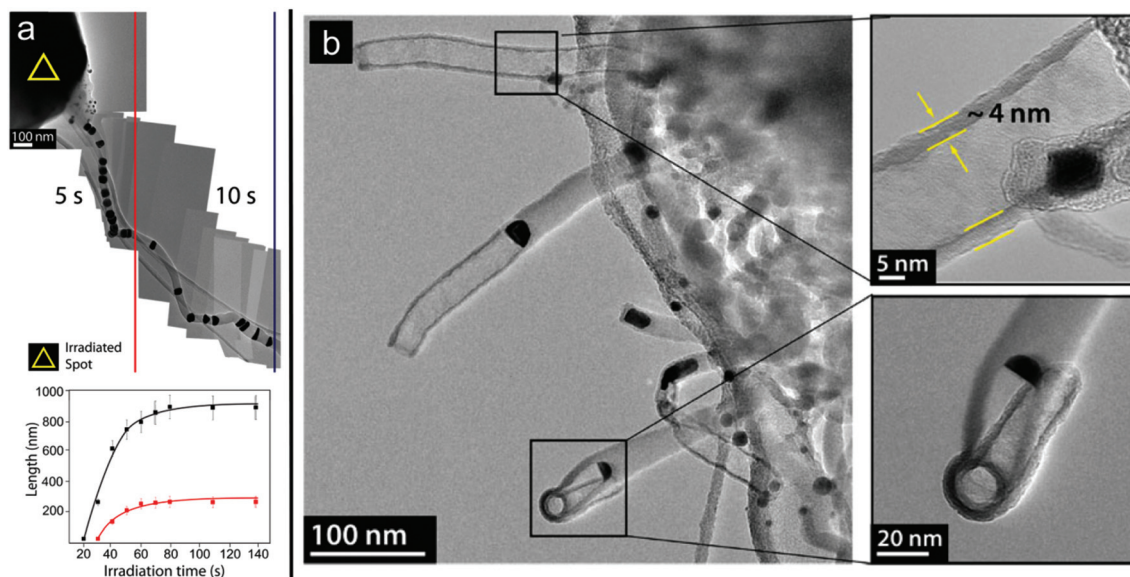
Fig. 8 (a) Superimposed collection of frames of the growth of a single B/BO$_X$ nanowires. The yellow triangle marks the position and size of the electron beam irradiating the precursor. Each position of the catalyst Au NP on the left side of the red line marks the length of the NW after consecutive irradiation periods of 5 seconds and of 10 seconds between the red and the blue line. The change of length of two distinct NWs (black and red curves) as a function of irradiation time are plotted in the graph below. (b) After extended periods of condensed irradiation the NWs can be turned into BO$_X$ nanotubes by delivering short periods of around 10 seconds of irradiation. The Au nanoparticles at the tips move gradually inwards as they consume the B core of the nanowires leaving only a nanotubular BO$_X$ shell. Panels (a) and (b) adapted with permission from ref. 100. Copyright American Chemical Society 2014.

material towards its edges. The force is exerted by a beam-induced field gradient, for instance, it can be established by an electrostatic field produced by localized charge accumulation. In such cases the feedstock material is made of ions produced by radiolysis reactions within the precursor. The growth of Cu and Ag nanowires extruded from their respective zeolites is in agreement with this general scheme (see Fig. 9a and b).[102–105] Cu/Ag ions are produced through radiolytic reduction reactions when the zeolites are irradiated with a condensed beam.

Beam-induced electric fields promote the migration of Cu/Ag ions towards structural mesopores created by structural disruptions within the zeolite. The mesopores act as Cu/Ag reservoirs. Some authors believe that negative charging of the metallic Cu/Ag might attract newly created positive ions, thus, accelerated the extrusion process of the nanowires.[105] One relevant feature of the synthesis process is that the crystallinity and morphology of the nanowires can be controlled by modulating the current density: low current density produced single-crystal straight nanowires while high current density results in twisted polycrystalline nanowires. Mayoral and Anderson achieved the growth of bimetallic Cu–Ag nanowires through this same method by irradiating a zeolite containing both metals.[105]

Ag filaments have also been extruded from α-Ag$_2$WO$_4$[106] and α-Ag$_2$MoO$_4$[107] crystals bombarded by an electron beam. Beam-induced reduction reactions produce the Ag feedstock material necessary for the growth of the filaments. Through theoretical considerations the authors deduce that the

reduction reactions initiates at positively charged AgO$_4$ clusters for the case of α-Ag$_2$WO$_4$ crystals (the process is analogous in the case of α-Ag$_2$MoO$_4$ although in this case the authors simply state that AgO$_6$ clusters are more prone to suffer reduction reactions). The clusters absorb beam electrons and that become polarized, thus, turning into chemically active moieties that react with neighboring AgO$_2$ clusters. The reduction reactions cause local amorphization as new AgO$_6$ clusters and Ag are produced. The authors then explain that the "the appearance of several defects in the crystal's surface" caused by "a reasonable amount of electrons" somehow drives the transport of Ag unto the growing filaments, however, they do not engage into explaining the details of exactly how this occurs.

Electric fields induced by local charging effect can also be used to promote the growth of SiO$_2$ nanorods out of porous silicon films. Solá et al. observed that edge regions of porous Si films (with a certain amount of SiO$_2$) made of a network of nanoparticles and short nanorods can be sintered by e-beam irradiation.[108] The sintered regions act as reaction sites for the extrusion of SiO$_2$ nanorods. The authors attribute the migration of feedstock material to superficial electrical fields building up as a consequence of the irradiation, however, they do not elaborate on details such as the polarity of the field or the charge of the feedstock material. On a complementary experiment the Solá et al. took the in situ produced SiO$_2$ nanorods to a TEM with poor vacuum conditions and observed that Si–C dendrites could grow from the tips of the nanorods upon irradiation. (Volatile hydrocarbons are thought to come from
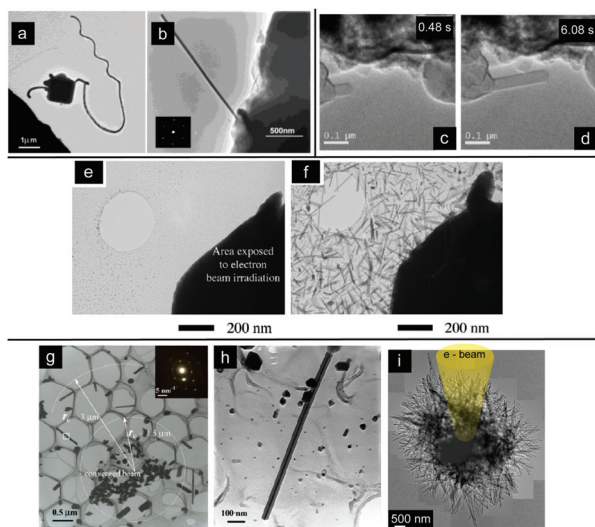
Fig. 9 (a) and (b) Crystalline Ag nanowires extruded from a piece of Ag zeolite irradiated by a focused electron beam. When the current density is raised the nanowires grow twisted and are polycrystalline as in (a) whereas if the current density is left constant and low (~20 pA cm^{-2}) the nanowires are straight single crystals as in (b). (c) and (d) Show the gradual growth of a Na nanorod being extruded from a NaCl crystal after 0.48 s and 6.08 s of e-beam irradiation respectively. (e) and (f) EBIF-like production of WO$_X$ nanowires. (e) WO$_X$ nanoparticles are expelled from a piece of flame-formed tungsten oxide fragment when subjected to 0.25 s of irradiation by a convergent beam. (f) WO$_X$ nanorods grow from the coalescence of the nanoparticles shown in (e) as the precursor WO$_X$ fragment is irradiated for 2.3 s. (g) and (h) Growth of Cu nanorods anchored on the lacey C at the periphery of the Cu agglomerated nanoparticles under the convergent beam. The size of the beam waist is indicated by the white circle, remarkably, some nanorods grow outside of it. The nanorods can grow longer than 1 micron as is shown in (h). (i) Aluminium borate nanowires protruding from a precursor particle after it has been exposed to a gradually convergent e-beam for a fraction of a second. The nanowires protrude in all directions in forming a structure that resembles a sea urchin. Panels (a) and (b) reproduced with permission from ref. 102. Copyright Wiley 2001. Panel (c) and (d) reproduced with permission from ref. 109. Copyright American Chemical Society 2012. Panels (e) and (f) reproduced with permission from ref. 116. Copyright Elsevier 2014. Panels (g) and (h) reproduced with permission from ref. 114. Copyright IOP Publishing all rights reserved 2004. Panel (i) reproduced with permission from ref. 119. Copyright Macmillan Publishers Limited 2016.

the diffusion pump.) The hydrocarbons are decomposed by the beam into volatile ions that aggregate at the nanorod's tips since the electric field is most intense in this spot.

Na nanorods can be extruded from NaCl grains through a combination of radiolysis and electric field generation inside a TEM. Neng *et al.* propose that the irradiation decomposes the NaCl crystals into a wide range of species, the majority of them being Na$^+$ and Na^0, as well as Cl$^-$ in a much smaller degree (see Fig. 9c and d).[109] The overall charge of the NaCl crystal becomes negative due to the massive outflow of positive Na ions that diffuse superficially and accumulate forming small Na nanocrystal. Accumulation of positive Na ions occurs at the Na/NaCl interface. Simultaneously negative charges are repelled due to the negative charge of the NaCl crystal and

aggregate at the nanocrystal's tip. This creates an electric field extending along the Na crystal whose polarity attracts newly generated Na cations to its tip, thus further instigating the growth of the Na nanorod.

A similar phenomenon is reported for Li nanorods extruding from irradiated LiCl crystals.[110] Here the electron beam decomposes the compound into solid Li and gaseous Cl (possibly through the K–F mechanism) which facilitates the aggregation and growth of Li nanostructures. The nanostructures can grow into elongated nanorods that are then coated with a thin LiCl layer that forms in the Cl atmosphere. However, the LiCl shell is subject to further decomposition which causes it to be easily permeable for the Li core. Under these circumstances the Li core can be rapidly released through the LiCl shell yielding a LiCl nanotube decorated by externally attached Li NPs as the final product of the process. It important to notice that although the decomposition of the LiCl crystal might produce charged ions there is no reference made to electrostatic effects affecting the growth of the nanostructures.

At times the physical causes behind the extrusion process are left essentially open for speculation. For instance, Yen *et al.* extruded cupper nanowires from CuCl microparticles coated with a thing polymethylpolysilane (PMPS) exposed to a convergent e-beam. When the process is carried out in "naked" CuCl particles EBIF is observed.[67] The precursors expel vast numbers of Cu nanoparticles making clear that the beam induces radiolysis reactions on the precursors. When the PMPS sheath is added EBIF is mitigated and Cu nanowires are obtained. The authors then speculate that the function of the sheath is to contain the outflow of Cu atoms. The confinement provided by the sheath promotes the coalescing of Cu NPs into Cu nanowires. The authors do not touch upon the driving force behind Cu diffusion; one could speculate that beam-induced heating might play a role as it is typical of EBIF reactions.

In other works, the *in situ* extrusion of nanowires is explicitly formulated as a sequence of physical events triggered beam-induced heating. This has been the case of extrusion of Ag-based nanowires inside SEMs. Li and coworkers produced SiO$_x$–Ag$_y$O offshoots from spherical SiO$_x$–Ag$_y$O particles by irradiating them with 5 kV electrons.[111] The nanowires grow fast (only after 5 s of irradiation) and intermittently reaching over 2.5 microns in length. Contrary to the extrusion processes presented before, here the growth occurs from the nanowires' base rather than through aggregation of feedstock material at their tips. The authors hypothesize that the material inside the precursor spheres is in a non-steady non-equilibrium state. The beam disrupts the material though heat generation thus increasing the internal pressure that ultimately drives the extrusion process. Umalas *et al.* studied the extrusion of Ag nanorods out of Ag NWs supported over a SiO$_2$ substrate and coated by a TiO$_2$ layer inside a SEM operated between 5 and 30 kV.[112] The substrates with the coated nanowires were annealed prior to the SEM studies. Optimal growth was obtained in samples annealed at 400 °C where the TiO$_2$ coating crystallized into a porous anatase phase. Also, the authors discovered that

a TiO_2 film thickness between 50 and 200 nm was necessary for growth. The authors explain the growth process in terms of in-built stresses due to the thermal expansion mismatch between the SiO_2 substrate, the Ag nanowires and the porous TiO_2 coating. Ag has the highest thermal coefficient followed by the TiO_2 coating and the SiO_2 at last. The Ag nanowires dilate as they are irradiated, this builds up a pressure that cannot be contained by the coating that has a smaller thermal coefficient. As a consequence the Ag nanowires get squeezed through the pores of the coating. The authors also speculate that in-built electric fields due to trapped electrons can further enhance the mobility of Ag ions towards the nanopores.

The last of the examples of *in situ* synthesis of nanowires through beam-induced extrusion corresponds to the case of pure Te nanowires grown from $Si_2Sb_2Te_5$ films coated by a 5 nm layer of SiO_2.[113] Interestingly, Te nanowires can be spontaneously "self-extruded" from such samples. The authors report that large numbers of nanowires had been observed after storing the samples for over two months. However, the action of the beam can instigate growth around 4 orders of magnitude faster than through spontaneous self-extrusion. The authors then explain that the beam accelerates the decomposition of $Si_2Sb_2Te_5$ into Sb_2Te_3, Si and Te. The Te filters through the SiO_2 coating and forms nanodots from where the nanowires grow. It is speculated that the extrusion is driven by the beam-induced release of a "special surface strain" retained in the films, *i.e.* through a kind of pressure-driven process. As mentioned above, there are some reports on the beam-driven synthesis of nanowires that can grow disconnected from their precursors (similar to EBIF). Some authors advocate for beam-induced heating as the main mechanism responsible for the growth of the nanowires. Wang *et al.* produced crystalline Cu nanorods by irradiating Cu grains with a convergent e-beam (see Fig. 9g and h). At the onset of the process, small Cu islands start to appear over the lacey C support in regions that lie outside the irradiated region.[114] These islands act as seeds for the growth of straight Cu nanorods as the grains continue to be irradiated. The authors hypothesize that the growth occurs thanks to the superficial migration of Cu atoms over the lacey C due to the creation of a thermal gradient induced by the e-beam. The highest temperature is generated on the precursor grains in the center of the irradiated region where the Cu precursor is produced. The atoms then diffuse to colder regions outside the beam spot, aggregate into islands and then promote the further growth of the Cu nanorods.

The majority of the remaining works in this subsection deal with the production of nanowires out of tungsten-based materials which are particularly sensitive to e-beam irradiation. Shen *et al.* obtained crystalline $W_{18}O_{49}$ nanowires can be obtained by irradiating core–shell $PbWO_4/WO_3$ microcrystals.[115] Upon irradiation the inner $PbWO_4$ core rapidly decomposes into $W_{18}O_{49}$ while the WO_3 shell remains stable. As the irradiation continues, the $W_{18}O_{49}$ filters through the WO_3 shell that becomes increasingly more porous due to beam-induced damage. Nanowires start to grow gradually

deposited over the lacey C that surrounds the precursor as the $W_{18}O_{49}$ feedstock slowly leaks through. The authors believe that the force behind $W_{18}O_{49}$ migration comes from atomic displacement through knock-on collisions between beam electrons and the precursor's core. Merchan-Merchan *et al.* observed a very rapid expulsion of W sub-oxide nanorods from micron-sized tungsten oxide fragments exposed to a convergent beam (see Fig. 9e and f).[116] During the first second of irradiation numerous nanoparticles are deposited over the lacey C film and grown into long nanorods reaching about 90% of their final length after this short irradiation time. Just as it is typical of EBIF reactions, the length of the nanorods diminishes as their distance to the precursor increases. The nanorods formation starts through the partial coalescence of spherical WO_X NPs that are nucleated almost instantaneously as W and O are released from the precursor. The further growth and smoothening of the nanorods occurs thanks to continued release of W and O due to beam-induced heating of the remaining precursor. The authors argue that the small size of the precursors reduces their melting temperature to the point where the beam can generate enough heat to sublimate and decompose it.

The work of Dawson *et al.* lies at the borderline between synthesis processes that resemble EBIF and global morphological changes induced over the precursor by the electron beam. The researchers produced WO_3 nanowires by irradiating a precursor consisting of WO_3 covered with a sheath of trimethylamine.[117] Large areas of the precursors rapidly break into bundles of WO_3 nanowires that get deposited over the surrounding lacey C support. The role of the trimethylamine sheath is crucial in this transformation, the authors explain that it acts as a kind of "molecular knife" that severs large precursor chunks turning them into nanowires. The trimethylamine attach to the WO_3 and weaken their bonds. However, the beam-induced reactions between the amine groups and the precursor that are likely to be responsible of ultimately breaking bonds within the precursor are not explicitly discussed.

Full global transformation of a irradiated WO_3 nanocrystals into WO_3 nanowires by the action of an electron beam was achieved by Sood and coworkers.[118] The experimenters observed a large-scale polymorphic reaction that occurs in a matter of seconds as a gradually converging beam irradiates an agglomeration of WO_3 nanocrystals turning it into a bundle of individual nanowires. The authors describe the process as a beam-triggered self-catalytic reaction that is only explained in broad terms: the phase of the nanocrystals is inherently metastable and the energy input provided by the beam is enough to drive the massive rearrangement necessary to produce more stable WO_3 nanowires. One can draw similarities between this phenomenon and the beam-induced crystallization process described by Qin and collaborators (see section 2.4).[50,51]

Gonzalez-Martinez *et al.* performed a similar experiment to that of Sood *et al.* but irradiating precursors that did not contained tungsten.[119] In this case the precursors were composed by round amorphous micron-sized particles containing Al, B

and O. The precursors quasi-instantaneously transformed into bundles of Al_5BO_9 NWs sticking out from an amorphous scaffold remnant from the original precursors, a structure that resembles a sea urchin (see Fig. 9i). The authors argue that the massive atomic rearrangement happens along lines similar to those sketched by Qin *et al.*[50,51] Beam-induced desorption of (mostly) oxygen generates interstitial free-volume gaps that enhance atomic rearrangement within the precursor. The Al_5BO_9 nanowires are thus the products that result from a crystallization process that ends once the atomic rearrangement is completed. Moreover, further growth can be instigated on those nanowires that by chance stick out supported over the lacey C film. The growth is achieved when the remaining scaffold is irradiated by the e-beam condensed into a nanometer-sized probe. Feedstock generation and transport is thought to occur through a process analogous to that explained for the growth of B/BO_X NWs (see section 4.1). Feedstock material is generated by well-localized charging taking place within the irradiated region. The accumulated charges generate a growing electric field that disrupts the specimen's structure driving cascades of positively charged ions (mainly B species) towards the tips of the growing nanowires to instigate further growth.

Two-dimensional nanostructures

Electron beams, particularly when highly focused, can produce significant topological modifications on thin TEM specimens. Thanks to tools such as the STEM feature in many TEMs it is possible to produce extended features with sub-nanometer width in materials such as graphene, BN and MoS_2 atomically thin sheets, *etc*. with a high degree of controllability. There are at least three different ways in which an electron beam can modify a bidimensional nanostructure, it can do so by rearranging its atomic structure or changing its topology and/or architecture at a local or global level. We review the available literature on these three kinds of electron beam-induced transformations of two-dimensional nanostructures in precisely the order listed above.

Atomic rearrangement in 2D nanostructures induced by electron beams

Beam-induced atomic rearrangement of bidimensional specimens can be viewed as a "synthesis" procedure when it yields a nanostructure with properties significantly different from those of the original film. This for instance is attained when large regions of an amorphous film crystallize under the influence of the electron irradiation. The process can rely on atomic displacements and sputtering (or knock-on damage), either one dominating over the other or both taking place simultaneously.

A typical example of large-scale crystallization through atomic displacement was demonstrated by Börrnert *et al.* while inducing graphitization in free-standing amorphous C films as well as on amorphous C layers suspended over graphene.[120] The action of an 80 kV beam induces the formation of C nano-onions on free-standing films, while, a similar procedure produces epitaxial transformation of amorphous C sitting over a graphene sheet into stacked graphene layers (the process can also be reproduced substituting the graphene substrate by an hexagonal BN sheet). The authors comment that the graphitization occurs through "inelastic electron scattering interactions" that promote the breaking of bonds in amorphous carbon which then reorganizes itself in a more stable sp^2 planar carbon allotrope. The rearrangement into graphene sheets is driven by van der Waals forces with the hexagonal network of the graphene support (or BN sheet).

An "inverse" transformation turning crystalline graphene into an amorphous "glassy" C sheet can also be obtained if sputtering events are included besides of beam-induced atomic displacements. Eder *et al.* gradually introduced on pristine graphene sheets by bombarding them with a 100 kV beam, which is slightly above the sputtering energy threshold of graphene (see Fig. 10a–c).[121] The "vitrification" of the graphene sheet is thought to proceed through the removal of atoms as well as through C–C bond rotations caused by the impacting electrons. The process gradually distorts the hexagonal pattern of the network by stochastically introducing heptagonal and pentagonal rings over large areas of the sheet.

An extensive review covering the formation of various defects, induced by electron beams in two dimensional materials has already been written by Sun *et al.*[122]

Small free-standing atomically-thin membranes of Fe and ZnO can also be built through a process relying on beam-induced atomic rearrangement and subsequent self-assembly. Zhao *et al.* studied the formation of Fe membranes extending over graphene pores (see Fig. 10d and e).[123] The precursors consisted on residual iron cluster deposits from the $FeCl_3$ etching agent used to transfer the CVD-grown graphene sheets onto the TEM grids. The Fe clusters move over the graphene sheet as they are continually impacted by 80 kV electrons; if they encounter a pore along their path then the clusters proceed to rapidly rearrange into an atomically thin membrane covering as much area of the pore as possible. The Fe membranes have a square lattice and remain stable during several minutes of irradiation before collapsing into a cluster once again.

Quang and collaborators used a similar approach to induce the formation of free-standing graphene-like ZnO membranes over graphene pores (see Fig. 10f and g).[124] The researchers used evaporated small ZnO clusters over a lacey C TEM grid previously loaded with graphene flakes. Small clusters (*ca.* 2 nm of diameter) continuously changed their atomic structure from crystalline to amorphous and *vice versa* for as long as they are irradiated. Simultaneously, the beam sputters C atoms from the underlying graphene flakes forming pores in the vicinity of the fluctuating ZnO clusters. The clusters then extend over the pores forming hexagonal graphene-like ZnO layers (or even bilayers) with Zn atoms coordinated to 3 O atoms and *vice versa*. The ZnO membranes fluctuate dynamically under the e-beam until they eventually erode due to the continuous irradiation.
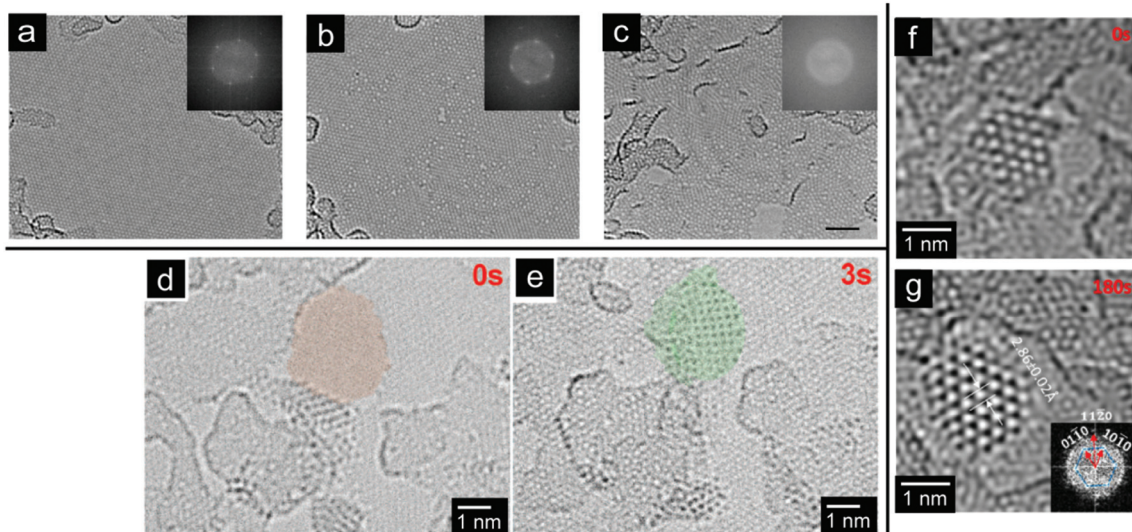
Fig. 10 (a) to (c) Graphene sheets irradiated at different current densities. (a) Low irradiation dose (1.25×10^8 e nm^{-2}), (b) moderate dose (2.94×10^9 e nm^{-2}) and (c) high dose (9.36×10^9 e nm^{-2}). The specimen irradiated at a higher dose shows a higher degree of beam-induced disordering (amorphization) as it can be noticed by observing the blurred out Fourier transformation pattern on the inset. (d) A small pore on a single-layer grapheme sheet is highlighted in red. A Fe cluster is seen right below the pore. (e) After 3 s of irradiation, the atoms of the Fe cluster have moved onto the pore forming an atomic-thick free-standing that completely covers the perforation. (f) A ZnO nanocrystallite sits on top of a grapheme flake. (g) The ZnO crystallite has rearranged into a flat single-sheet ZnO layer with an hexagonal configuration. Panels (a) to (c) reproduced with permission from ref. 121. Copyright Nature Publishing Group 2013. Panels (d) and (e) reproduced with permission from ref. 123. Copyright American Association for the Advancement of Science 2014. Panels (f) and (g) reproduced with permission from ref. 124. Copyright American Chemical Association 2015.

Synthesis of one dimensional features through selective carving of bidimensional materials

Focused e-beams can be used to "drill" point-like holes and/or well-defined carvings when moved along thin planar films. The size/width of the features is directly related to the dimensions of the beam profile and their shape follows the trajectory of the scanning beam. Although this process is fundamentally destructive, one can designate it as a synthesis process if the focus is put on the material remaining on the bidimensional substrate. For example, it is possible to carve large neighboring ridges separated by a thin constriction that can be identified as a nanoribbon. In other words, the carving process has been used to synthesize a nanoribbon bridging two separated areas of a bidimensional nanostructure. These types of *in situ* lithographic processes are based on inducing concentrated sputtering or ablation along well-defined tracks extending over the substrate. Graphene substrates constitute the material most commonly subjected to electron beam carving; nevertheless, the process has also been applied to two-dimensional materials such as BN, MoS$_2$ and MoSe$_2$ sheets.

Fischbein and Drndic fabricated nanopores, ridges and wider gaps in multilayered graphene sheets by a process of localized beam-induced ablation (see Fig. 11a–c).[125] The experimenters focused the 200 kV e-beam to get a beam probe with a diameter of around 1 nm (0.3 pA nm^{-2}) and used it to scan samples composed from 1 to 20 layers of graphene at a speed of around 1 s nm^{-2}. Pores could be "poked" after leaving the probe static for over 5 seconds. Linear ridges were carved by

slowly dragging the electron probe over it. By carving progressively wider parallel ridges the researchers fabricated 5 nm wide graphitic nanoribbons connecting two planar sections of the specimen. Lu *et al.* machined nanometric constrictions (from 1 to 700 nm wide) by carving previously synthesized graphene ribbons using a condensed 200 kV electron beam.[126] The initial graphene ribbons were loaded on top of a pair of Au electrodes put into a customized TEM grid. This allowed to perform electrical characterizations of graphene constrictions as a function of their width.

The technique developed by Fischbein *et al.* was driven to its extreme by several groups. Jin *et al.*[127] and Chuvilin *et al.*[128] independently and simultaneously managed to produce linear C chains by further removing edge atoms from nanoribbons produced by carving bidimensional C substrates (see Fig. 11d–f). The first team used commercial multilayered graphite nanoflakes as starting material. The first step of the process consisted on gradually sputter down the multilayered flakes by removing graphene layers one-by-one using a highly condensed electron beam (100 A cm^{-2}) of either 80 or 120 kV. Once the flakes have been converted into graphene nanoribbons extending over two neighboring holes the current density was reduced down to 4 A cm^{-2} in order to reduce the rate of radiation damage. The beam was then used to scan over the edges of the nanoribbon in order to gradually remove edge C atoms in order to produce a single atom C chain. The approach employed by Chuvilin *et al.* is essentially equivalent with the exception that the starting precursor material was single-layer graphene instead of multilayered flakes; thus,
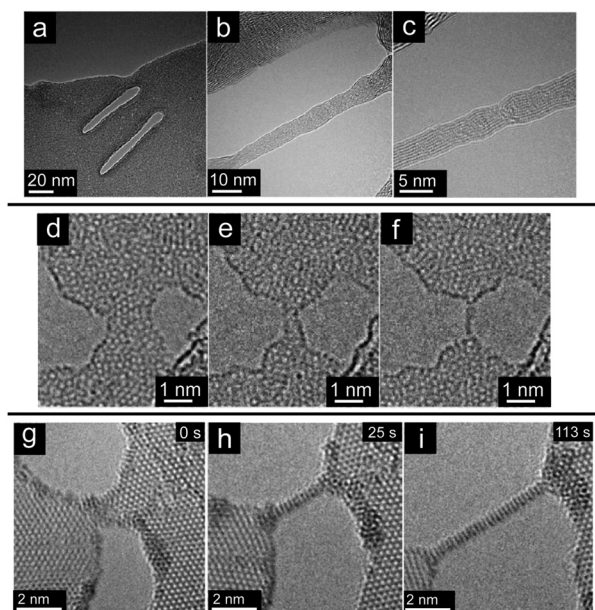
Fig. 11 (a) to (c) Carving of a thin graphitic nanoribbon out of few layer graphene. (a) Two 6 nm broad parallel lines carved into a few-layer graphene sheet by a condensed 200 kV e-beam. (b) The lines are broadened until they are separated by a graphene bridge with a width of around 5 nm. (c) Higher resolution micrograph of the graphene nanoribbon showing that it is made of stacked graphene layers. (d) to (f) Production of a single atom C chain our of a graphene nanoribbon sputtered by an e-beam. (d) A graphene nanoribbon sculpted out of a single-layer grapheme sheet. (e) Further sputtering reduces de constriction down to a sub-nanometer wide nanoribbon. (f) A double-stranded carbon chain is finally obtained as the sputtering process continues. (g) to (i) Production of a Mo_5S_4 nanoribbon through e-beam carving. (g) Holes sputtered out from a MoS_2 sheet forming a thin constriction bridging two sides of the flake. (h) A short Mo_5S_4 nanoribbon is obtained after 25 s of irradiation. (i) Further sputtering increases the length of the nanoribbon. Panels (a) to (c) reproduced with permission from ref. 125. Copyright American Institute of Physics 2008. Panels (d)–(f) reproduced with permission from ref. 127. Copyright American Physical Society 2009. Panels (g) to (i) reproduced with permission from ref. 131. Copyright American Chemical Society 2009.

skipping the initial thinning down step performed by Jin *et al.* Interestingly, in this work the researchers registered the existence of transitional constrictions (below 1 nm in width) dominated by carbon pentagons and heptagons that are surprisingly stable under the irradiating beam. Atomic C chains were also produced by Börrnert *et al.* by advancing a programmable protocol to carve patterns of arbitrary shapes over few layer graphene sheets.[14] Linear trajectories could be traced by a 200 kV STEM probe by adjusting the total current of the probe (selecting the size of the condenser aperture and the alignment of the C_S corrector) and programming the scan speed (dwell time) necessary to successfully cut through all the graphene layers. Thin graphene constrictions could be fabricated in this way, Subsequently the researchers set the microscope to TEM mode and operate it at 80 kV to selectively remove edge atoms of the constriction in order to produce thin nanoribbons and atomic C chains.

Algara-Siller *et al.* performed a two-step protocol analogous to that of Börrnert *et al.* to carve by-layer graphene and create single-walled C nanotube (SWCNT) constrictions.[129] The authors first used a 300 kV STEM probe to produce thin nanoribbon constrictions. Once the nanoribbons were carved the experimenters switch the microscope to TEM mode and proceeded to gradually sputter away edge atoms. The nanoribbon starts to zip-up into a SWCNT with an elliptical cross-section as the gradual sputtering narrows its width down.

The control carving of nanoribbons through sputtering has also been successfully performed in bidimensional materials other than graphene. Monolayer materials such as dichalcogenide compounds such as MoS_2 (molybdenum disulfide) have been subjected to similar processes. K. Liu *et al.* first successfully poked nanopores in MoS_2 sheets with a condensed beam arguing that such structures could be useful as DNA translocation devices.[130] Soon afterwards, X. Liu and coworkers extended the protocol to produce Mo_5S_4 out of MoS_2 monolayers (see Fig. 11g–i).[131] At first, the electron beam was highly focused (40 A cm^{-2}) to produce large holes separated by a thin constriction *via* knock-on damage. Afterwards, the current density of the beam was lowered down in order to selectively sputter atoms from the constriction's edges in order to produce thin nanoribbons. The authors note that the nanoribbons suffer a spontaneous phase transition as their width is reduced below 1 nm. Their stoichiometry changes from MoS_2 to Mo_5S_4 due to the comparatively higher susceptibility of S atoms to be removed by collisions with the beam electrons. Through this process the researchers were able to obtain nanoribbons with a sub-nanometer width of around 0.35 nm.

Lin *et al.* bombarded yet more dichalcogenide monolayers with a relatively low energy STEM probe (60 kV) to produce a series of flexible nanowires.[132] The team of researchers used the probe remove atoms from $MoSe_2$, MoS_2, and WSe_2 monolayers in order to produce MoSe, MoS and WSe nanowires respectively. The removal of atoms occurs through what the authors call "ionization etching" in which prolonged irradiation generates vacancies that grow into larger holes mainly due to a combination of energy transfer and repulsive interactions between ionized atoms. Nanoribbons and/or nanoribbon networks assemble themselves separating contiguous holes. Upon further irradiation the nannoribbons transform into thicker nanowires through a redeposition process of the atoms etched away from their edges. It is important to notice that the stoichimetry of the nanowires is different from that of their monolayer precursors, this has a strong effect on their conducting properties: the dichalcogenide monolayers are semiconducting while the nanowires are metallic (a fact that is made evident due to the much higher stability of the nanowires under prolonged irradiation). The authors thus disagree about the stoichiometry of Mo_5S_4 nanoribbons reported by X. Liu and coworkers, instead, they advocate for a MoS stoichiometry.

The last monolayer material that has been subjected to sputtering machining by electron beam irradiation is hexagonal boron nitride (hBN). However, hBN sheets are insulators and B as well as N have a lower knock-on damage threshold in compari-

son to C, therefore, hBN sheets are easily damaged under 80 kV irradiation (which is the most widely used low voltage limit used during TEM studies). Characteristic triangular holes grow in irradiated hBN sheets.[133–137] The holes are drilled rapidly and rather uncontrollably which makes selective removal of edge B or N atoms a (so far) unachievable task. Thus, thin constrictions such as nanoribbons or nanowires have not been fabricated out of irradiated hBN monolayers. At most, Ryu et al. report the observation of transient B–N chains existing in-between two growing holes.[137]

There is at least one example of a semi-destructive mechanism to produce one-dimensional features with an arbitrary shape on top of graphene sheets. Zhang et al. used a 300 kV STEM probe to "draw" letters made of amorphous carbon on top of single-layer graphene.[138] The "writing" process begins with the sputtering of C atoms leaving broken dangling C–C bonds along the trajectories traced by the probe. The dangling bonds attract environmental C species, simultaneously, the probe continues to produce inelastic scattering events on the graphene sheet that induces local disorder as well as an ultra-low yield of secondary electrons. The secondary electrons play a leading role in the C deposition process and the inelastic interactions induce crosslinking among the deposited carbon and the graphene substrate that results in local amorphization. The researchers could draw 1 nm wide letters using this approach.

Global topographical transformations on bidimensional structures induced by electron irradiation

There are at least two examples of works in which electron beam irradiation are able to induce a global change in the topology of thin hybrid nanostructures. In both cases an originally planar structure is folded and eventually completely rolled under the action of the irradiating e-beam. Such processes generally rely on the release/activation of internal stresses in the bidimensional structures triggered by electron collisions.

Liu and collaborators produced conducting C films supported by Cu TEM grids and then "sprinkled" with a variety of different nanostructures such as: Cu_2ZnSnS_4 NPs, Au nanorods, Te NWs, disordered and aligned Ag NWs and graphene.[139] The researchers noted that the supported "C-based nanocomposite" films curl and roll under the action of a 100 kV e-beam after cutting a slit on them (see Fig. 12a–c). The rolling process is driven by gradual residual strain relieved by the impacting electrons until the composites turn into nearly cylindrical multilayered structures with diameters ranging from hundreds of nanometers to tens of microns. The role of the electrons is to release the elastic energy stored within the underlying film substrate, however, it is not specified if this happens through elastic or inelastic collision events.

Jiang et al. fabricated membranes composed of Au nanoparticles interconnected by organic ligands and found that they could undergo a similar rolling process while exposed to electron irradiation (see Fig. 12d–f).[140] The membranes formed floating on a water droplet exposed to air (they formed at the water/air interface) and where subsequently washed and dried. The membranes bent and rolled towards the water-facing side when they were exposed to the 3 kV e-beam of a SEM (regardless of the direction of the incoming beam with respect to the membrane). This phenomenon is due to the
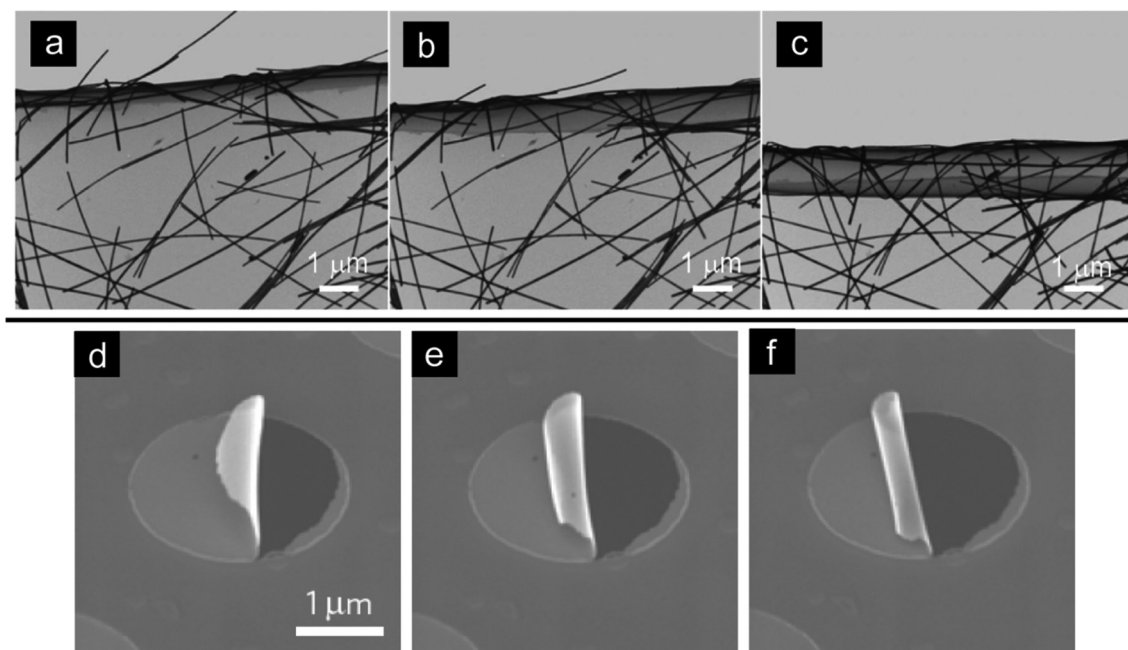
Fig. 12 (a) to (c) Gradual rolling up of an amorphous carbon film "sprinkled" with Ag nanowires while it is being irradiated by a 100 kV e-beam. (d) to (f) Circular membrane of Au NPs interconnected by organic ligands rolling up into a tube under the action of a 3 kV electron beam of a SEM. Panels (a) to (c) reproduced with permission from ref. 139. Copyright American Chemical Society 2012. Panels (d) to (f) reproduced with permission from ref. 140. Copyright Macmillan 2015.

slightly higher ligand coverage of the Au NPs on their water-facing side. The electron beam breaks C–H, C–C and C–S bonds leading to the formation of C=C bonds which pull the nanoparticles closer together. When the e-beam irradiates the membrane a differential strain is established due to the asymmetric ligand distribution. The strain is higher on the water-facing side due to the lower ligand density, therefore, the membrane tends roll over this face. Multi-walled cylinders with diameters of a couple of hundreds or nanometers are the end product of the beam-induced rolling process.

Other geometries

Electron beams have been used to sculpt nanostructures of more irregular or quasi-fractal geometries through processes driven by charge-induced electric fields directing the flow of charged feedstock material Fonseca *et al.* report the growth of multi-branched Si nanostructures (nanotrees) out of amorphous porous Si films.[141] The first transformation consists on beam heating-induced densification of the irradiated edges of the porious Si film (similar to what was observed by Solá *et al.* during the beam-induced production of Si nanorods). These densified regions constitute the active growth sites of the nanotrees. The growth of the nanotrees is instigared by irradiating the densified regions by extended periods of time. Broader trunks of around 30 to 100 nm in length sprout a large collection of thinner branches. The authors propose that the growth proceeds through the generation of internal electric fields that are enhanced at the growing tips of the branches. Local changes in the concentration of charged feedstock material generates multiple bumps at the growth front of the nanotrees, each one then acting as a competing for the acquiescence of feedstock material since the electric field gradient is stronger at their position. The growing fronts multiply through this process causing numerous bifurcations that give rise to the tree-like nanostructures.

Cho *et al.* were also able to produce nanotrees by applying a similar irradiation protocol over several Si-based polymers (see Fig. 13).[142] Two types of nanotrees were identified according to their morphology. Type I had a wide trunk and thin nanowire-like branches and were produced at lower current densities (up to 30 μA cm^{-2}) while the type II were fractal-like assemblies of spherical nanoclusters and were synthesized at current densities above 40 μA cm^{-2}. Both kinds of nanotrees were composed of a mixture of SiC and SiO$_2$ phases. The feedstock material necessary for the nanotrees growth is produced through the decomposition (radiolysis) of the base polymer by the beam electrons. Several oxycarbine molecules are generated some of which are released as vapors and some others that are able to superficially diffuse through the polymer and the nanotrees. The nanotrees accumulate charges which generate an electric field that is particularly intense at the tips of the branches. The field attracts the feedstock species which get progressively deposited therefore extending the length of the branches and promoting overall growth.
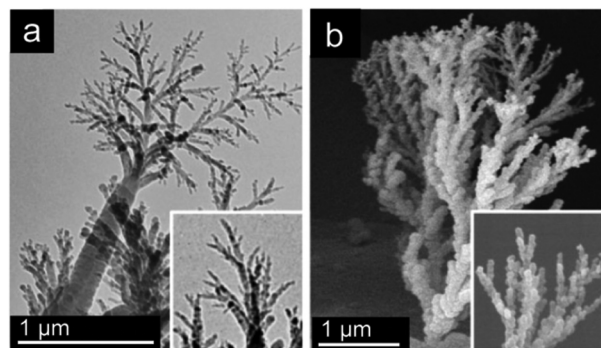

Fig. 13 Branched nanostructures with two distinctive morphologies produced by irradiated silicon-based inorganic polymer precursors. (a) Thick and straight trunk-like rods with thin branches produced at current densities below 10 μA cm^{-2}. (b) Profusely branched arrangement of spherical nanostructures produced at current densities between 10–30 μA cm^{-2}. Panels (a) and (b) reproduced with permission from ref. 142. Copyright Wiley 2006.

Conclusions

Direct synthesis of nanostructures using only (or mainly) an electron beam is a relatively recent and very promising manufacturing technique. Currently, TEM is at the forefront of the research in this area of investigation. Its capability for real-time observation during *in situ* experimentation has proven to be a great advantage when it comes to our understanding of the fundamental processes leading to the growth/formation mechanisms of different kinds of nanostructures. In addition, it is also proving its worth as a tool for the machining of nanostructures. On the other hand, TEM is not suited to large scale synthesis as might be required for industrial applications. A new kind of specialized machinery must be assembled if the electron-beam induced synthesis technique is to be put forward as a viable alternative for the production of nanostructures at an industrial scale. Nevertheless, several of the synthesis approaches highlighted in this review could be used for the direct assembly of devices with relatively complex architectures. For instance, nanowires and multibranched structures whose growth depends on the migration of charged feedstock species could be made to grow towards nearby electrodes (suspended or supported) held at a certain electrostatic potential. Selective precipitation of crystalline nanoparticles by the action of focused beams of crystalline can produce complex patterns of metallic islands embedded in amorphous insulating matrixes, an architecture that might be useful for charge storage applications. The field is currently on its initial stages and there are reasons to be optimistic about its prospects as a valuable method for a wide range of applications and the generation of new technologies. Moreover, the ability to synthesize nanostructures inside a TEM allows for unprecedented and real-time feedback which provides a level of insight not available with conventional *ex situ* synthesis approaches.

Acknowledgements

Notes and references

1 A. Botman, J. J. L. Mulders and C. W. Hagen, *Nanotechnology*, 2009, **20**, 372001.

2 M. Huth, F. Porrati, C. Schwalb, M. Winhold, R. Sachser, M. Dukic and J. Adams, *Beilstein J. Nanotechnol.*, 2012, **3**, 597–619.

3 J. D. Wnuk, S. G. Rosenberg, J. M. Gorham, W. F. van Dorp, C. W. Hagen and D. H. Fairbrother, *Surf. Sci.*, 2011, **605**, 257–266.

4 W. F. van Dorp and C. W. Hagen, *J. Appl. Phys.*, 2008, **104**, 081301.

5 T. W. Kim, J. W. Shin, J. Y. Lee, J. H. Jung, J. W. Lee, W. K. Choi and S. Jin, *Appl. Phys. Lett.*, 2007, **90**, 051915.

6 J.-H. Shim, N.-H. Cho, J.-G. Kim and Y.-J. Kim, *J. Non-Cryst. Solids*, 2009, **355**, 2339–2344.

7 A. A. Tseng, K. Chen, C. D. Chen and K. J. Ma, *IEEE Trans. Electron. Packag. Manuf.*, 2003, **26**, 141–149.

8 M. Altissimo, *Biomicrofluidics*, 2010, **4**, 026503.

9 K. Furuya, *Sci. Technol. Adv. Mater.*, 2008, **9**, 014110.

10 R. F. Egerton, P. Li and M. Malac, *Micron*, 2004, **35**, 399–409.

11 L. W. Hobbs, in *Introduction to Analytical Electron Microscopy*, ed. J. J. Hren, J. I. Goldstein and D. C. Joy, Plenum Press, New York, USA, 1987, pp. 399–445.

12 R. F. Egerton, R. McLeod, F. Wang and M. Malac, *Ultramicroscopy*, 2010, **110**, 991–997.

13 B. W. Smith and D. E. Luzzi, *J. Appl. Phys.*, 2001, **90**, 3509–3515.

14 F. Börrnert, L. Fu, S. Gorantla, M. Knupfer, B. Büchner and M. H. Rümmeli, *ACS Nano*, 2012, **6**, 10327–10334.

15 M. L. Knotek and P. J. Feibelman, *Surf. Sci.*, 1979, **90**, 78–90.

16 M. L. Knotek, *Rep. Prog. Phys.*, 1984, **47**, 1499–1561.

17 P. H. Citrin, *Phys. Rev. Lett.*, 1973, **31**, 1164–1167.

18 T. A. Carlson and M. O. Krause, *Phys. Rev. Lett.*, 1965, **140**, A1057–A1064.

19 H. Iwasaki, T. Yoshinobu and K. Sudoh, *Nanotechnology*, 2003, **14**, R55–R62.

20 E. H. Adem, D. L. Seymour and E. B. Pattinson, *Surf. Sci.*, 1984, **141**, 1–12.

21 M. R. McCartney, P. A. Crozier, J. K. Weiss and D. J. Smith, *Vacuum*, 1991, **42**, 301–308.

22 D. J. Smith, M. R. McCartney and L. A. Bursill, *Ultramicroscopy*, 1987, **23**, 299–304.

23 J. W. Rogers and M. L. Knotek, *Appl. Surf. Sci.*, 1982, **13**, 352–364.

24 A. Bachmatiuk, A. Dianat, F. Ortmann, H. T. Quang, M. O. Cichocka, I. Gonzalez-Martinez, L. Fu, B. Rellinghaus, J. Eckert, G. Cuniberti and M. H. Rümmeli, *Chem. Mater.*, 2014, **26**, 4998–5003.

25 J. Cazaux, *Ultramicroscopy*, 1995, **60**, 411–425.

26 F. J. Pijper and P. Kruit, *Phys. Rev. B: Condens. Matter*, 1991, **44**, 9192–9200.

27 J. Cazaux, *Microsc. Microanal. Microstruct.*, 1995, **6**, 345–362.

28 T. Takamori, R. Messier and R. Roy, *J. Mater. Sci.*, 1973, **8**, 1809–1816.

29 V. D. Das and P. J. Lakshmi, *Phys. Rev. B: Condens. Matter*, 1988, **37**, 720–726.

30 R. K. Sharma, S. K. Bansal, R. Nath, R. M. Mehra, K. Bahadur, R. P. Mall, K. L. Chaudhary and C. L. Garg, *J. Appl. Phys.*, 1984, **55**, 387–394.

31 L. Nikolova, T. LaGrange, M. J. Stern, J. M. MacLeod, B. W. Reed, H. Ibrahim, G. H. Campbell, F. Rosei and B. J. Siwick, *Phys. Rev. B: Condens. Matter*, 2013, **87**, 064105.

32 P. Kern, Y. Müller, J. Patscheider and J. Michler, *J. Phys. Chem. B*, 2006, **110**, 23660–23668.

33 Z. C. Li, H. Zhang and Y. B. Xu, *Mater. Sci. Semicond. Process.*, 2004, **7**, 19–25.

34 J. Murray, K. Song, W. Huebner and M. O'Keefe, *Mater. Lett.*, 2012, **74**, 12–15.

35 W. J. Weber and J. W. Wald, *J. Nucl. Mater.*, 1986, **138**, 196–209.

36 R. C. Ewing and T. H. Headly, *J. Nucl. Mater.*, 1983, **119**, 102–109.

37 W. J. Weber and Hj. Matzke, *Mater. Lett.*, 1986, **5**, 9–16.

38 A. Meldrum, L. A. Boatner and R. C. Ewing, *J. Mater. Res.*, 1997, **12**, 1816–1827.

39 M. O. Ruault, J. Chaumont, J. M. Penisson and A. Bourret, *Philos. Mag. A*, 1984, **50**, 667–675.

40 G. Lulli, P. G. Merli and P. G. M. V. Antisari, *Phys. Rev. B: Condens. Matter*, 1987, **36**, 8038–8042.

41 F. Corticelli, G. Lulli and P. G. Merli, *Philos. Mag. Lett.*, 1990, **61**, 101–106.

42 I. Jenčič, M. W. Bench, I. M. Robertson and M. A. Kirk, *J. Appl. Phys.*, 1995, **78**, 974–982.

43 X. Yang, R. Wang, H. Yan and Z. Zhang, *Mater. Sci. Eng.*, 1997, **B49**, 5–13.

44 R. Nakamura, M. Ishimaru, H. Yasuda and H. Nakajima, *J. Appl. Phys.*, 2013, **113**, 064312.

45 F. Lu, Y. Shen, X. Sun, Z. Dong, R. C. Ewing and J. Lian, *Acta Mater.*, 2013, **61**, 2984–2992.

46 M. Kaiser, L. van Pieterson and M. A. Verheijen, *J. Appl. Phys.*, 2004, **96**, 3193–3198.

47 B. J. Kooi, W. M. G. Groot and J. Th. M. De Hosson, *J. Appl. Phys.*, 2004, **95**, 924–932.

48 T. Zhang, Z. Song, M. Sun, B. Liu, S. Feng and B. Chen, *Appl. Phys. A*, 2008, **90**, 451–455.

49 I.-T. Bae, Y. Zhang, W. J. Weber, M. Higuchi and L. A. Giannuzzi, *Appl. Phys. Lett.*, 2007, **90**, 021912.

50 W. Qin, T. Nagase and Y. Umakoshi, *Acta Mater.*, 2009, **57**, 1300–1307.

51 W. Qin, J. A. Szpunar and Y. Umakoshi, *Acta Mater.*, 2011, **59**, 2221–2228.

52 W. D. Pyrz, S. Park, T. Vogt and D. J. Buttrey, *J. Phys. Chem. C*, 2007, **111**, 10824–10828.

53 M. A. Caldwell, B. Haynor, S. Aloni, D. F. Ogletree, H.-S. P. Wong and J. J. Urban, *J. Phys. Chem. C*, 2010, **114**, 22064–22068.

54 J. Frantz, J. Tarus, K. Nordlund and J. Keinonen, *Phys. Rev. B: Condens. Matter*, 2001, **64**, 125313.

55 P. J. Herley and W. Jones, *Suppl. Z. Phys.*, 1993, **D26**, S159–S161.

56 B. G. Yacobi, *Phys. Rev. B: Condens. Matter*, 1980, **22**, 1007–1009.

57 K. P. O'Donnell and X. Chen, *Appl. Phys. Lett.*, 1991, **58**, 2924–2926.

58 Q. Ru, *Appl. Phys. Lett.*, 1997, **71**(1792), 159–161.

59 J. Ghatak, W. Guan and G. Möbus, *Nanoscale*, 2012, **4**, 1754–1759.

60 P. del Angel, J. H. Rodriguez-Hernandez, A. Garcia-Borquez and J. A. Montoya de la Fuente, *Catal. Today*, 2013, **212**, 194–200.

61 B. Lu, C. Wang and Y. Zhang, *Appl. Phys. Lett.*, 1997, **70**, 717–719.

62 Z. W. Pan, Z. R. Dai and Z. L. Wang, *Appl. Phys. Lett.*, 2002, **80**, 309–311.

63 W. D. Pyrz, S. Park, D. A. Blom, D. J. Buttrey and T. Vogt, *J. Phys. Chem. C*, 2010, **114**, 2538–2543.

64 M. R. Buck, I. T. Sines and R. E. Schaak, *Chem. Mater.*, 2010, **22**, 3236–3240.

65 T. Gnanavel and G. Möbus, *J. Nanopart. Res.*, 2012, **14**, 683.

66 K. Li and F.-S. Zhang, *J. Nanopart. Res.*, 2010, **12**, 1423–1428.

67 M.-Y. Yen, C.-W. Chiu, F.-R. Chen, J.-J. Kai, C.-Y. Lee and H.-T. Chiu, *Langmuir*, 2004, **20**, 279–281.

68 X.-W. Du, M. Takeguchi, M. Tanaka and K. Furuya, *Appl. Phys. Lett.*, 2003, **82**, 1108–1110.

69 J. W. Shin, J. Y. Lee, Y. S. No, T. W. Kim, W. K. Cho and S. Jin, *Nanotechnology*, 2008, **19**, 295303.

70 N. Jiang, J. Qiu and J. Silcox, *Appl. Phys. Lett.*, 2000, **77**, 3956.

71 M. M. Sabri, R. J. Hand and G. Möbus, *J. Mater. Res.*, 2015, **30**, 1914–1924.

72 S. Sepulveda-Guzman, N. Elizondo-Villarreal, D. Ferrer, A. Torres-Castro, X. Gao, J. P. Zhou and M. Jose-Yacaman, *Nanotechnology*, 2007, **18**, 335604.

73 S. H. Kim, Y.-S. Choi, K. Kang and S. I. Yang, *J. Alloys Compd.*, 2007, **427**, 330–332.

74 S. P. Singh and B. Karmakar, *J. Nanopart. Res.*, 2011, **13**, 3599–3606.

75 J.-U. Kim, S.-H. Cha, K. Shin, J. Y. Jho and J.-C. Lee, *J. Am. Chem. Soc.*, 2005, **127**, 9962–9963.

76 R. J. T. Houk, B. W. Jacobs, F. El Gabaly, N. N. Chang, A. A. Talin, D. D. Graham, S. D. House, I. M. Robertson and M. D. Allendorf, *Nano Lett.*, 2009, **9**, 3413–3418.

77 B. W. Jacobs, R. J. T. Houk, B. M. Wong, A. A. Talin and M. D. Allendorf, *Nanotechnology*, 2011, **22**, 375601.

78 B. W. Jacobs, R. J. T. Houk, M. R. Anstey, S. D. House, I. M. Robertson, A. A. Talin and M. D. Allendorf, *Chem. Sci.*, 2011, **2**, 411–416.

79 C. Díaz, M. L. Valenzuela, D. Bravo, C. Dickinson and C. O'Dwyer, *J. Colloid Interface Sci.*, 2011, **362**, 21–32.

80 X. Zhou, Z. Yan and X. Han, *Mater. Res. Bull.*, 2014, **50**, 118–127.

81 G. Xie, Q. Zhang, D. V. Louzguine-Luzgin, W. Zhang and A. Inoue, *Mater. Trans.*, 2006, **47**, 1930–1933.

82 Q. Su, G. Du and B. Xu, *Mater. Lett.*, 2014, **120**, 208–211.

83 T. Kizuka, *Jpn. J. Appl. Phys.*, 2001, **40**, L1061–L1064.

84 Y. Kojima and T. Kato, *Nanotechnology*, 2008, **19**, 255605.

85 D. Ugarte, *Nature*, 1992, **359**, 707–709.

86 G. Lulli, A. Parisini and G. Mattei, *Ultramicroscopy*, 1995, **60**, 187–194.

87 M. S. Zwanger, F. Banhart and A. Seeger, *J. Cryst. Growth*, 1996, **163**, 445–454.

88 Q. Ru, M. Okamoto, Y. Kondo and K. Takayanagi, *Chem. Phys. Lett.*, 1996, **259**, 425–431.

89 T. Oku, G. Schmid and K. Suganuma, *J. Mater. Chem.*, 1998, **8**, 2113–2117.

90 T. Oku, G. Schmid, K. Suganuma, Q. Sun and Y. Kawazoe, *Mol. Cryst. Liq. Cryst.*, 2000, **340**, 95–100.

91 B. S. Xu and S.-I. Tanaka, *Acta Mater.*, 1998, **46**, 5249–5257.

92 H. E. Troiani, A. Camacho-Bragado, V. Armendariz, J. L. Gardea Torresday and M. Yacaman, *J. Chem. Mater.*, 2003, **15**, 2003.

93 A. Chuvilin, U. Kaiser, E. Bichoutskaia, N. A. Besley and A. N. Khlobystov, *Nat. Chem.*, 2010, **2**, 450–453.

94 F. Banhart, M. Zwanger and H.-J. Muhr, *Chem. Phys. Lett.*, 1994, **231**, 98–104.

95 O. Stéphan, Y. Bando, A. Loiseau, F. Willaime, N. Shramchenko, T. Tamiya and T. Sato, *Appl. Phys. A*, 1998, **67**, 107–111.

96 D. Goldberg, Y. Bando, O. Stéphan and K. Kurashima, *Appl. Phys. Lett.*, 1998, **73**, 2441–2443.

97 P. Ramasamy, S. Guha, E. S. Shibu, T. S. Sreeprasad, S. Bag, A. Banerjee and T. Pradeep, *J. Mater. Chem.*, 2009, **19**, 8456–8462.

98 B. Wang, Y. H. Yang and G. W. Yang, *Nanotechnology*, 2006, **17**, 5916–5921.

99 L. Zhang, Q. Feng, A. Nie, J. Ma, H. Wang, J. Liu and Y. Fang, *Mater. Lett.*, 2015, **156**, 134–137.

100 I. G. Gonzalez-Martinez, S. M. Gorantla, A. Bachmatiuk, V. Bezugly, J. Zhao, T. Gemming, J. Kunstmann, J. Eckert, G. Cuniberti and M. H. Rümmeli, *Nano Lett.*, 2014, **14**, 799–805.

101 T. Uchiyama, H. Yoshida, Y. Kuwauchi, S. Ichikawa, S. Shimada, M. Haruta and S. Takeda, *Angew. Chem., Int. Ed.*, 2011, **50**, 10157–10160.

102 M. J. Edmondson, W. Zhou, S. A. Sieber, I. P. Jones, I. Gameson, P. A. Anderson and P. P. Edwards, *Adv. Mater.*, 2001, **13**, 1608–1611.

103 P. Anderson, M. J. Edmondson, P. P. Edwards, I. Gameson, P. J. Meadows, S. R. Johnson and W. Zhou, *Anorg. Allg. Chem.*, 2005, **631**, 443–447.

104 X. Ding, G. Briggs, W. Zhou, Q. Chen and L.-M. Peng, *Nanotechnology*, 2006, **17**, S376–S380.

105 A. Mayoral and P. A. Anderson, *Nanotechnology*, 2007, **18**, 165708.

106 E. Longo, L. S. Cavalcante, D. P. Volanti, A. F. Gouveia, V. M. Longo, J. A. Varela, M. O. Orlandi and J. Andrés, *Sci. Rep.*, 2013, **3**, 1676.

107 J. Andres, L. Gracia, P. Gonzalez-Navarrete, V. M. Longo, W. Avansi, D. P. Volanti Jr., M. M. Ferrer, P. S. Lemos, F. A. La Porta, A. C. Hernandes and E. Longo, *Sci. Rep.*, 2014, **4**, 5391.

108 F. Solá, O. Resto, A. Biaggi-Labiosa and L. F. Fonseca, *Nanotechnology*, 2007, **18**, 405308.

109 W. Neng, L.-T. Sun, X.-H. Hu, Y.-Y. Zhu, Z. Lin, X. Tao, H.-C. Bi, S. Jun and F.-Z. Dong, *Cryst. Growth Des.*, 2012, **12**, 3899–3905.

110 W. Neng, M. Martini, S. Wei-Ning, X. Ling, S. Li-Tao and S. Yuting, *CrystEngComm*, 2013, **15**, 7872–7878.

111 C. Li, X. Zhang and Z. Zhang, *Mater. Lett.*, 2004, **58**, 3573–3577.

112 M. Umalas, S. Vlassov, B. Polyakov, L. M. Dorogin, R. Saar, I. Kink, R. Lõhmus, A. Lõhmus and A. E. Romanov, *J. Cryst. Growth*, 2015, **410**, 63–68.

113 Y. Cheng, X. D. Han, X. Q. Liu, K. Zheng, Z. Zhang, T. Zhang, Z. T. Song, B. Liu and S. L. Feng, *Appl. Phys. Lett.*, 2008, **93**, 183113.

114 P.-I. Wang, Y.-P. Zhao, G.-C. Wang and T.-M. Lu, *Nanotechnology*, 2004, **15**, 218–222.

115 G. Shen, Y. Bando, D. Golberg and C. Zhou, *J. Phys. Chem. C*, 2008, **112**, 5856–5859.

116 W. Merchan-Merchan, M. F. Farahani and Z. Moorhead-Rosenberg, *Micron*, 2014, **57**, 23–30.

117 G. Dawson, W. Zhou and R. Blackley, *Phys. Chem. Chem. Phys.*, 2011, **13**, 20923–20926.

118 S. Sood, K. Kisslinger and P. Gouma, *J. Am. Ceram. Soc.*, 2014, **97**, 3733–3736.

119 I. G. Gonzalez-Martinez, T. Gemming, R. Mendes, A. Bachmatiuk, V. Bezugly, J. Kunstmann, J. Eckert, G. Cuniberti and M. H. Rümmeli, *Sci. Rep.*, 2016, **6**, 22524.

120 F. Börrnert, S. M. Avdoshenko, A. Bachmatiuk, I. Ibrahim, B. Büchner, G. Cuniberti and M. H. Rümmeli, *Adv. Mater.*, 2012, **24**, 5630–5635.

121 F. R. Eder, J. Kotakoski, U. Kaiser and J. C. Meyer, *Sci. Rep.*, 2013, **4**, 4060.

122 L. Sun, F. Banhart and J. Warner, *MRS Bull.*, 2015, **40**, 29–37.

123 J. Zhao, Q. Deng, A. Bachmatiuk, S. Gorantla, A. Popov, J. Eckert and M. H. Rümmeli, *Science*, 2014, **343**, 1228–1232.

124 H. T. Quang, A. Bachmatiuk, A. Dianat, F. Ortmann, J. Zhao, J. H. Warner, J. Eckert, G. Cunniberti and M. H. Rümmeli, *ACS Nano*, 2015, **11**, 11408–11413.

125 M. D. Fischbein and M. Drndić, *Appl. Phys. Lett.*, 2008, **93**, 113107.

126 Y. Lu, C. A. Merchant, M. Drndic and A. T. C. Johnson, *Nano Lett.*, 2011, **11**, 5184–5188.

127 C. Jin, H. Lan, L. Peng, K. Suenaga and S. Iijima, *Phys. Rev. Lett.*, 2009, **102**, 205501.

128 A. Chuvilin, J. C. Meyer, G. Algara-Siller and U. Kaiser, *New J. Phys.*, 2009, **11**, 083019.

129 G. Algara-Siller, A. Santana, R. Onions, M. Suyetin, J. Biskupek, E. Bichoutskaia and U. Kaiser, *Carbon*, 2013, **65**, 80–86.

130 K. Liu, J. Feng, A. Kis and A. Radenovic, *ACS Nano*, 2014, **8**, 2504–2511.

131 X. Liu, T. Xu, X. Wu, Z. Zhang, J. Yu, H. Qiu, J.-H. Hong, C.-H. Jin, J.-X. Li, X.-R. Wang, L. Sun and W. Guo, *Nat. Commun.*, 2013, **4**, 1776.

132 J. Lin, O. Cretu, W. Zhou, K. Suenaga, D. Prasai, K. I. Bolotin, N. T. Cuong, M. Otani, S. Okada, A. R. Lupini, J. C. Idrobo, D. Caudel, A. Burger, N. J. Ghimire, J. Yan, D. G. Mandrus, S. J. Pennycook and S. T. Pantelides, *Nat. Nanotechnol.*, 2014, **9**, 436–442.

133 C. Jin, F. Lin, K. Suenaga and S. Iijima, *Phys. Rev. Lett.*, 2009, **102**, 195505.

134 J. C. Meyer, A. Chuvilin, G. Algara-Siller, J. Biskupek and U. Kaiser, *Nano Lett.*, 2009, **9**, 2683–2689.

135 N. Alem, R. Erni, C. Kisielowski, M. D. Rossell, W. Gannett and A. Zettl, *Phys. Rev. B: Condens. Matter*, 2009, **80**, 155425.

136 J. H. Warner, M. H. Rümmeli, A. Bachmatiuk and B. Büchner, *ACS Nano*, 2010, **4**, 1299–1304.

137 G. H. Ryu, H. J. Park, J. Ryou, J. Park, J. Lee, G. Kim, H. S. Shin, C. W. Bielawski, R. S. Ruoff, S. Hong and Z. Lee, *Nanoscale*, 2015, **7**, 10600–10605.

138 W. Zhang, Q. Zhang, M.-Q. Zhao and L. T. Kuhn, *Nanotechnology*, 2013, **24**, 275301.

139 J.-W. Liu, J. Xu, Y. Ni, F.-J. Fan, C.-L. Zhang and S.-H. Yu, *ACS Nano*, 2012, **6**, 4500–4507.

140 Z. Jiang, J. He, S. A. Deshmukh, P. Kanjanaboos, G. Kamath, Y. Wang, S. K. R. S. Sankaranarayanan, J. Wang, H. M. Jaeger and X.-M. Lin, *Nat. Mater.*, 2015, **14**, 912–917.

141 L. F. Fonseca, O. Resto and F. Solá, *Appl. Phys. Lett.*, 2005, **87**, 113111.

142 S. O. Cho, E. J. Lee, H. M. Lee, J. G. Kim and Y. J. Kim, *Adv. Mater.*, 2006, **18**, 60–65.